National Research Council
National Institute of Optics
Largo Fermi 6
50125 Firenze, Italy
Tel. +39.055.23081

Prepared by Luca Palchetti
Sesto Fiorentino Research Unit
Via Madonna del Piano 10
50019 Sesto Fiorentino (Firenze)
Email. luca.palchetti@ino.cnr.it
Tel. +39.055.5226311

Contribution from
Marco Barucci, Claudio Belotti, Giovanni Bianchini, Francesco D'Amato, Gianluca Di Natale, Alessio Montori, Silvia Viciani, CNR-INO
Samuele Del Bianco, Marco Gai, Flavio Barbara, CNR-IFAC
Ralf Sussmann, Markus Rettinger, Hannes Vogelmann, KIT/IMK-IFU
Christian Rolf, Dina Khordakova, Forschungszentrum Jülich, Germany
Bertrand Cluzet, Univ. Grenoble Alpes, Univ. de Toulouse, Météo-France, CNRS, Centre d'Etudes de la Neige, Grenoble, France

D8 – Final Report

ESA Contract No. 4000123691/18/NL/LF

"FIRMOS - Technical Assistance for a Far-Infrared Radiation Mobile Observation System (EE9 Forum)"

1 INTRODUCTION

The FIR (far-infrared) is the longest wavelength region of the infrared spectrum with frequency from 667 cm^{-1} (or equivalently 15 μm wavelength) down to 10 cm^{-1} (1000 μm). The FIR contains more than 50% of the energy emitted by the Earth toward the space and it is modulated by some of the most relevant components of the climate system which are the water vapour, carbon dioxide, clouds, and snow surface emissivity. The characterization of the FIR radiative properties of these components is therefore fundamental to understand the Earth radiation budget and to improve the accuracy of climate models. Nevertheless, systematic and global measurements of the FIR are still lacking from the space due to technical challenges. To fill this observational gap, a space mission named FORUM (Far-infrared-Outgoing-Radiation Understanding and Monitoring) has been recently selected by ESA as the ninth Earth Explorer mission to be launched in 2025-2026 timeframe. This mission will measure with high accuracy the spectrum of the outgoing infrared radiation from 100 to 1600 cm^{-1} (100-6.25 μm), covering for the first time the FIR portion of the spectrum.

In preparation of this mission, a new facility named FIRMOS (Far-Infrared Radiation Mobile Observation System) has been developed for field applications from both ground-based and airborne platforms to check with real measurements the sounding capability provided by FIR observations.

Because the high opacity of the atmosphere in the FIR spectral region at ground level, caused by the high concentration of water vapour, the sounding of the FIR with ground-based observations is possible only from high altitude sites where the water vapour content is sufficiently low to allow transparency of the atmosphere below 667 cm^{-1}. This requires the deployment of FIR instrumentation on high mountain sites around 3000 m AMSL or more. Also, observations during the winter-time are preferred in order to have the water vapour content at its seasonal minimum and improving the capability to sound down to the lowest wavenumber region close to 250 cm^{-1}. The sounding of wavenumbers lower than 250 cm^{-1} is only possible from airborne platforms, high-altitude aircrafts or balloons, flying in the upper troposphere or the lower stratosphere (see Section 7).

In this report we describe the field campaign performed with FIRMOS at the end of 2018 beginning of 2019 from the Zugspitze Observatory at about 3000 m of altitude and the results obtained from the Level 2 data analysis. The FIRMOS instrument, developed in 2018 at CNR-INO, is described in Section 2. The Zugspitze Observatory facilities and the instrument deployment are described in Section 0 and 4, respectively. Section 5 is devoted to the results obtained in clear-sky conditions and Section 6 in cloudy conditions. Finally, in Section 7 the roadmap for upgrading FIRMOS high-altitude balloon-borne application is depicted.

2 THE FIRMOS INSTRUMENT

FIRMOS ESA-funded technical and ground-based deployment followed the already ongoing activities for a similar instrument under development in the framework of the Italian ASI SCIEF programme, this allowed to respond to the field campaign schedule constrains, and to achieve a cost-effective solution. The FTS (Fourier transform spectrometer) for FIRMOS was developed starting from the SCIEF prototype design of a laboratory interferometer and a reference black body source (BB) ready at laboratory level. Under the ESA support, this instrument was adapted and completed with all the required sub-systems and protections necessary for the FIRMOS deployment in ground-based field campaigns.

2.1 OPTOMECHANICAL LAYOUT

The final configuration of the FTS and subsystems in FIRMOS are shown in Figure 1.

The proposed FTS uses an interferometric layout with double-input and double-output ports in Mach-Zehnder configuration, which increases the measurement reliability and calibration precision. One of the two input ports looks continuously at the reference BB which is at the same temperature of the instrument while the other input looks at the scene selection mirror, allowing to choose between the scene to be measured and the calibration sources.
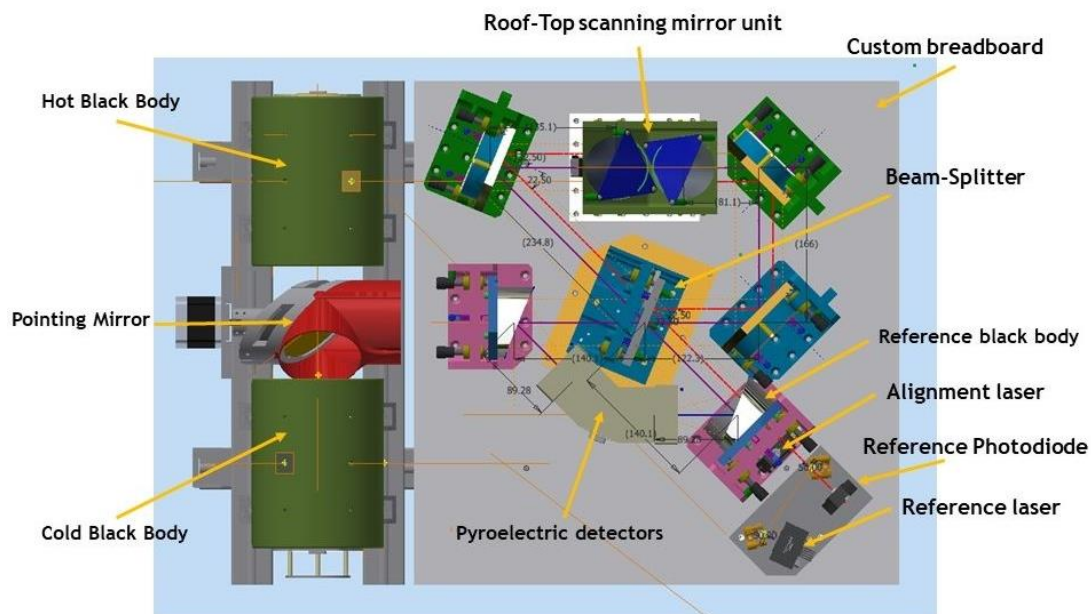

Figure 1. Final configuration of the FIRMOS Opto-Mechanics.

The two output ports feed two room-temperature uncooled pyroelectric DLATGS (deuterated, L-alanine doped triglycine sulphate) detectors, each one in the focal plane of an off-axis parabolic mirror (PDU (Pyroelectric Detector Unit)).

The beam splitters (BS) are wideband PET (Polyethylene terephthalate)-Germanium-coated. Weight and power consumption (70 kg/70 W) are low enough for the instrument to be suitable for field deployment both on ground-based sites and on-board of stratospheric balloon platforms.

Table 1 main characteristics of the FIRMOS instrument.

Interferometer configuration	Mach-Zehnder type
Beam splitters	Ge-coated PET film (thickness 0.65 μm/1.5 μm)
Detectors	uncooled DLATGS pyroelectric (Selex ES P5180)
Spectral coverage	150-1000 cm^{-1} (blind in some narrow absorption bands due to the PET BS substrate). The limit at 150 cm^{-1} is due to the CsI window used on the detectors where are the limit at 1000 cm^{-1} is due to the degradation of performance caused by the flatness error present on the available BSs.
Maximum spectral resolution	0.25 cm^{-1}
Optical throughput	0.0063 cm^2 sr
Beam aperture FOV (Field of view)	22.4 mrad
Line of sight	Zenith, Nadir, slanted angle
Acquisition time	≥ 10 s
Weight and power Consumption	About 70 kg / 60 W

2.2 REFERENCE SOURCES FOR CALIBRATION

The instrument requires two calibration BB (Black body) sources, one heated at about 60°C – HBB (Hot black body), one cooled CBB (Cold black body) at a few degrees below the ambient temperature around 13-15 °C, and one reference source at ambient temperature RBB (Reference black body).

RBB is within the interferometer and at the same temperature, no stringent requirements are posed on its emissivity, therefore it was used a simple black coated corrugate surface, made by machined aluminium in multi pyramidal form, to achieve a good thermal equilibrium with the interferometer beam splitters.

In order to maximise the calibration BBs' emissivity and reduce the calibration error the HBB and CBB were carefully designed adopting a cavity geometry shaped as a cylinder and an inner cone, resulting in an emissivity better than 0.99 for the whole spectral range. The calibration BBs were assembled in 3D-printed shells, made of co-polyester plastic in the case of the CBB, the HBB one is made of heat-resistant carbon-fiber-reinforced nylox plastic. The inner surfaces of the shells were overlaid aluminium coated reflective thermal insulation foils to minimise the thermal exchange. Moreover, the internal cavity is in aluminium in order to reduce the weight for the field application, the surface was black coated the absolutely light-diffusing surface absorbs 98 % of the light, independent of the angle of incidence.

The BBs controllers were made in-house, each one reads 4 temperature sensors: a high accuracy (30mK) PT-100 for temperature reading; a high resolution (500 µK) NTC sensor for temperature stabilisation; two one-wire Dallas DS18B20 digital thermometers to check temperature homogeneity.

The controller was calibrated by means of a Lakeshore 218 Temperature Monitor resulting in a 200mK positive offset that is factored in the calculation of the calibration error. The thermal stability and homogeneity were assessed analysing the PT100 sensors and Dallas thermometers, resulting in 1 mK for the CBB and 8.5 mK for the HBB

Table 2, Calibration black bodies characteristics.

Measured Characteristics	CBB	HBB
Working Temperature	13-15 ^{0}C	60 ^{0}C
Temperature stabilisation	1 mK	8.5 mK
Measurement accuracy	30 mK	30 mK
Thermal gradient	0.3 K	0.3 K

2.3 BEAM SPLITTERS

The BS (Beam splitter) were manufactured in house using 1.5 µm PET film deposited with 650 nm of germanium. Unfortunately, even the best available samples do not have a good flatness, the measured flatness error is about 2 µm peak-valley (PV) which resulted in a relevant degradation of the overall performance above 1000 cm^{-1}. However, between 100 and 700 cm^{-1} the components work well with a moderate degradation in the expected NESR (Noise equivalent spectral radiance) (see Figure 2). A flatness error of 0.3 µm PV (peak-valley) or less would be needed to have a negligible efficiency degradation.
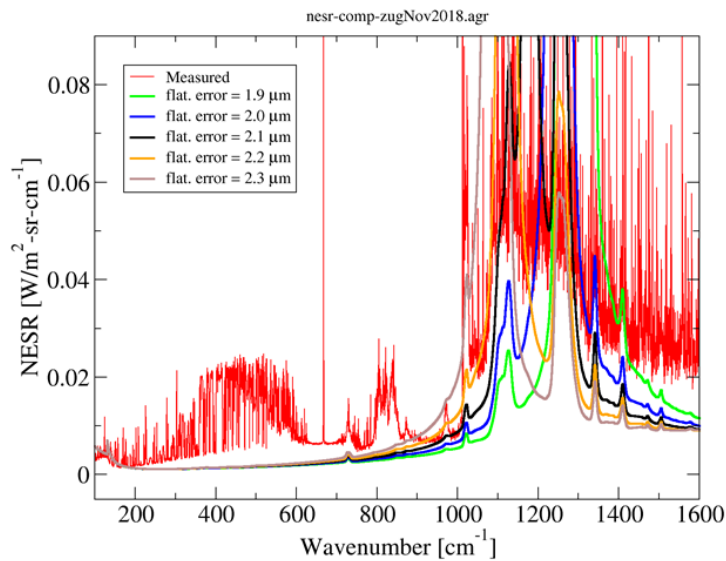

Figure 2 Comparison between measured and simulated NESR considering different values of BS flatness peak-valley error.

As a result of the BS flatness error, the useful spectral range covered by FIRMOS was limit to 1000 cm^{-1}.

2.4 SPECTRAL MEASUREMENTS (LEVEL 1 ANALYSIS)

The double input port configuration chosen for the FIRMOS interferometer design, makes it possible to measure the difference spectrum between the input atmospheric radiance and a stable RBB source (Carli et al. 1999, Palchetti et al. 1999) to maximise the flexibility of the interferometer to balance the input signals and reduce the dynamic range of the interferogram. The selected optical configuration makes the second input port accessible and controllable because it looks continuously at the RBB source.

The double output port is also an advantage because it provides redundancy and monitoring capabilities. The two ports can be used to cover the same spectral range and increase by averaging the signal to noise ratio. The two output ports give complementary interferograms (opposite signs), deviation from this complementarity can be used to quantify the self-interferogram due to BS self-emission. This effect is also minimised by using the RBB at the same temperature of the instrument (Bianchini et al., 2009).

The Level 1 data analysis allows to calculate the calibrated spectrum starting from the acquired interferograms, one per output channel. Level 1 is divided into 3 steps: Level 1a (Uncalibrated spectra), Level 1b (Calibrated spectra), Level 1c (Calibrated spectrum averaged of the two output channels).

2.4.1 Fourier Transform (Level 1a)

The Level 1a processing algorithm is described in the flowchart of Figure 3. It involves different algorithms to obtain the uncalibrated spectrum from the raw interferogram: filtering, resampling, FT transformation, and calibration of housekeeping data. 2 uncalibrated spectra are obtained for each interferometric scan.

2.4.2 Calibration (Level 1b)

The radiometric calibration performed on FIRMOS follows the procedure outlined in (Bianchini et al., 2008) and it is summarised here below.

Radiometric calibration is obtained by calculating the instrumental response using the onboard calibration sources HBB and CBB. The instrument output is proportional to the difference of the two inputs with a wavenumber dependent complex response function F that in general is different for the two inputs (as well as for the two outputs). This implies that the calibration must be performed by changing the observed scene while keeping the second (reference) sources RBB as constant as possible. Complex spectra are used in order to consider at best for possible phase errors at full spectral resolution. Thus, in the analysis the multiplicative phase error, that is applied to the observed source, it can be separated from the additive phase of the other components, such as the self-interferogram (even if the latter is expected to be small because of the uncooled detectors).

In these conditions for each output channel, the frequency dependent uncalibrated spectrum S(σ), defined as the complex Fourier transform, is related to the spectrum L(σ) of the observed scene, through the following relationship:

$$S(\sigma) = F1(\sigma)L(\sigma) - F2(\sigma)L_{RBB}(\sigma)$$

where L_{RBB} is the radiance of the reference black-body RBB and F1/F2 are the complex response functions.
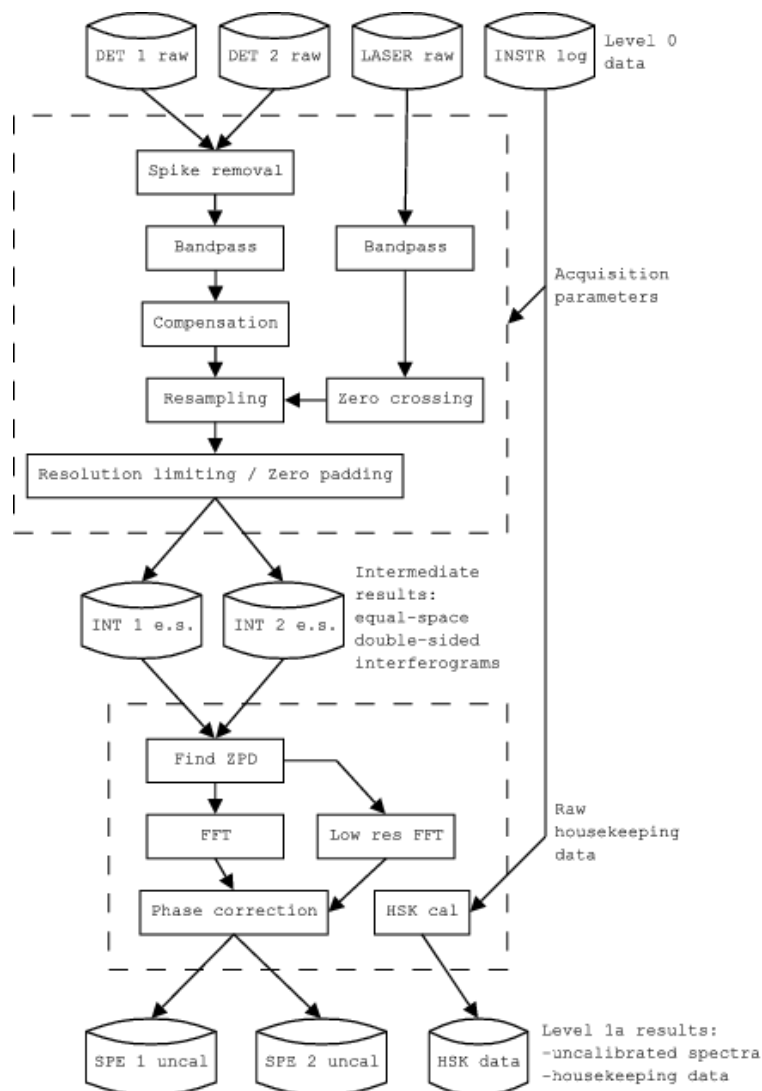
Figure 3. Level 1a analysis flow diagram.

The calibration of L is then obtained from a two-point radiometric calibration procedure performed by means of the measurement of the radiance of two calibration black-bodies, HBB (about 340 K) and CBB (at about 288 K), which allows to calculate F1 and F2.

All the parameters in the equation are frequency dependent and generally different for each of the two outputs. However, in practice, finding the exact phase relation among sources can be a tricky job in presence of large beam splitter (BS) absorption or curvature errors, which introduces an anomalous phase effect. If this effect is large, it can distort the spectrum especially at high frequency and where the BS absorbs.

Once the calibration functions F are calculated, the calibrated radiance $L(\sigma)$ is calculated from the uncalibrated spectrum $S(\sigma)$ and the theoretical expression of $L_{RBB}(\sigma)$ following equation:

$$L(\sigma) = R \left\{ \frac{s(\sigma)}{F1(\sigma)} + \frac{F2(\sigma)}{F1(\sigma)} L_{RBB}(\sigma) \right\}$$

In general, all the quantities used in the calibration procedure, are complex, and only in the last calculation, the real part of the result is taken, obtaining, as needed, the measured spectrum as a real quantity. This is the most accurate calibration procedure to consider phase error distortions.

The Level 1b follows the flow diagram shown in Figure 4. The calibration of FIRMOS is performed using 4 calibration acquisitions, in which the instrument looks at the internal calibration BB sources (2 acquisitions of CBB and 2 of HBB), and it is repeated every 4 sky observations. For each interferometric scan looking at the atmosphere, 2 calibrated spectra are obtained, one per each interferometric scan.
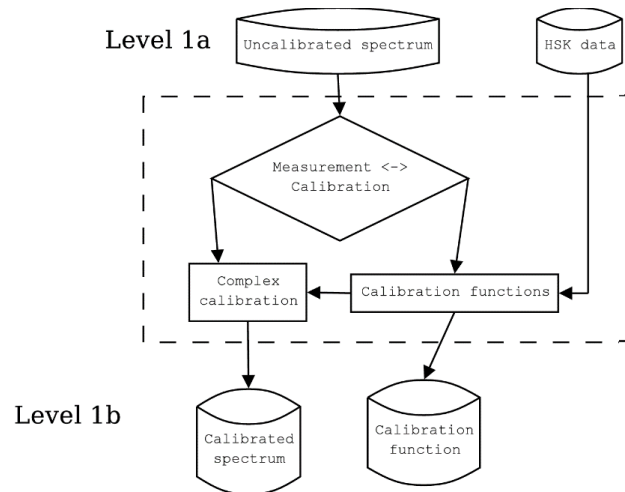

Figure 4. Flow diagram of the Lvel1b calibration procedure.

2.4.3 Averages (Level 1c)

The Level 1c provides the average spectra for a measurement sequence composed of the 4 sky observations. Level 1c provides both the average spectra separated for the two output channels and an average of the two channels. All the averages are weighted with the noise estimate.

In addition to the calibrated spectrum, the FIRMOS Level 1c products include the 1σ uncertainty estimates of the associated random NESR, spectrally (independent from one spectral channel to the other), and the CalErr (calibration errors), spectrally correlated but independent from one measurement to the other.

On each output channel, NESR can be generally obtained from the error propagation in the calibration equation and, for the average of 4 sky measurements with 4 calibrations, as performed with FIRMOS, it is given by

$$NESR = \sqrt{\frac{1}{4} + \left(\frac{S}{S_{HBB} - S_{CBB}} \right)^2} \frac{\Delta S}{F}$$

where ΔS is the 1σ uncertainty on the uncalibrated spectrum S, and F is F1≈F2.

CalErr is obtained through the error propagation of the temperature accuracy error measured on the reference blackbodies. If we consider the case in which the temperature error of each reference blackbody is independent and that the corresponding uncertainty on the theoretical Planck emission is given by ΔLHBB, ΔLCBB, and ΔLRBB, we obtain the calibration error ΔL from the following equation:

$$CalErr = \sqrt{\Delta L_{RBB}{}^2 + \left(\frac{S}{S_{HBB} - S_{CBB}}\right)^2 \left(\Delta L_{CBB}{}^2 + \Delta L_{CBB}{}^2\right)}$$

In the case of FIRMOS also with a very conservative value of 0.3 K for the temperature accuracy of the blackbody, the error ΔL is smaller than the NESR.

As an example of performance, Figure 5 shows the Level 1c products for one single channel.
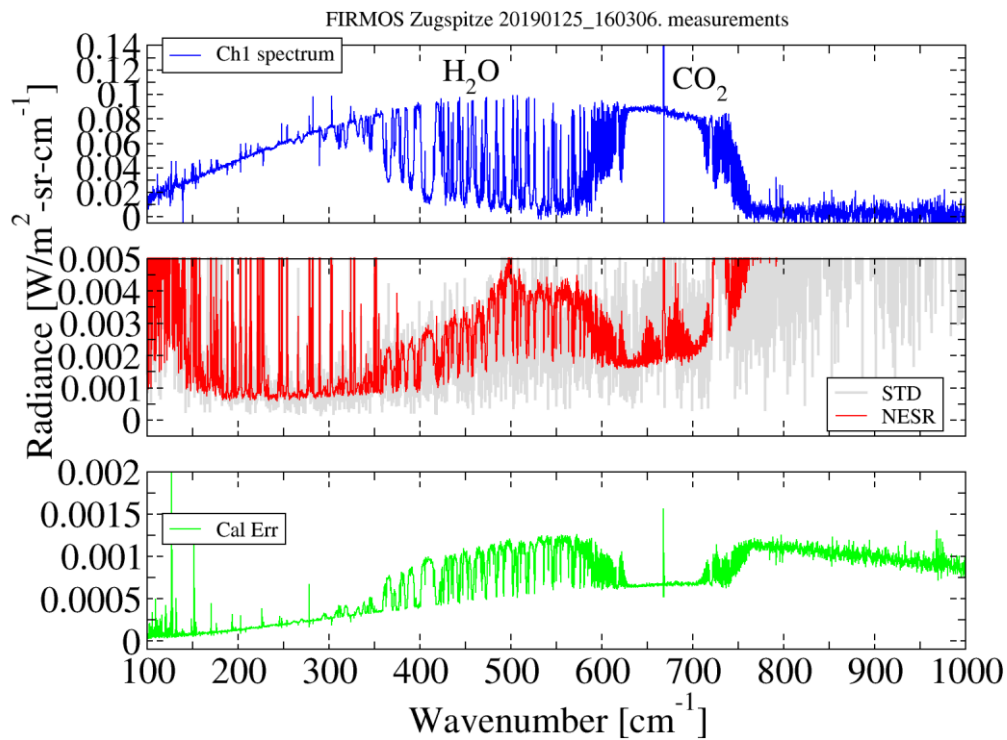

Figure 5. Example of Level 1c product for channel 1

3 ZUGSPITZE OBSERVATORY

A field campaign was performed between the end of 2018 and beginning of 2019 at the Alpine observatory of Mt. Zugspitze (Germany) at about 3000 m altitude. The goal of this campaign was to provide evidence of the FIR capability to retrieve IWV (Integrated Water Vapour) as well as vertical profiles of water vapour and temperature, and cirrus cloud properties with FIRMOS, and to perform a side-by-side radiance validation.

Very dry atmospheric conditions are a prerequisite for such FIR spectrometric studies due to the otherwise saturated spectral regions. At the Zugspitze we frequently encounter extremely dry atmospheric conditions (min IWV = 0.1 mm, median IWV = 2.3 mm, for details see Sussmann et al., 2016). The minimum IWV levels at the Zugspitze (0.1 mm) are approximately a factor of 40 lower than at typical lowland midlatitude sites. Note, that in this respect the Zugspitze is comparable to the driest sites in the world, i.e. remote locations like the Atacama Desert or polar stations.

The Zugspitze Observatory is reachable via cable car within 10 min from car parking and offers a suitable infrastructure for the deployment of FIRMOS due to the presence of a complementary and comprehensive set of instrumentation. This provides independent information of the observed atmospheric and cloud states to be used as truth for the comparison with FIRMOS.

The Zugspitze Observatory consists of two stations, the Summit station (47.421 °N, 10.986 °E, 2962 m AMSL) (see Figure 6 left picture) and the UFS (Environmental Research Station Schneefernerhaus) (Lat. 47.417°N, Lon. 10.980°E, 2675 m AMSL), on the south slope of Mt. Zugspitze, 680 m southwest, and 300 m below the Summit (see Figure 7).
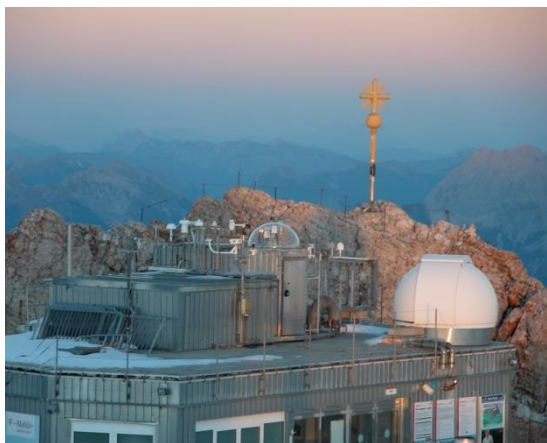

Figure 6. Summit observatory with solar FTIR dome (left) and E-AERI (right) at the Mt. Zugspitze, Germany.

At the summit station KIT operates an E-AERI system covering the FIR and mid infrared and a solar FTIR system covering both the mid infrared and the near infrared (Figure 6 right picture). KIT operates also lidar systems for aerosols, water vapour and temperature at the Schneefernerhaus. The advantage of mounting the lidar systems at Schneefernerhaus and the FTIR systems at the summit is that the onset of the measured lidar profiles is typically ≈300 m above the laser, which coincides with the location of the FTIR spectrometers at

the summit. FIRMOS was installed on the Summit which provided very dry conditions in wintertime with total integrated water vapour as low as 1 kg/m^2 in the period November 2018 - February 2019 when the campaign took place.
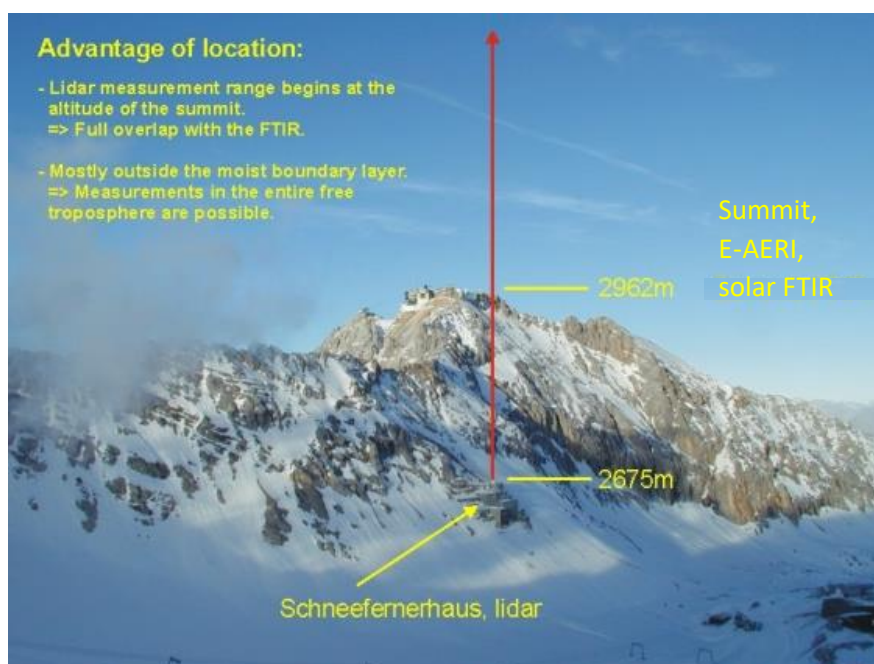

Figure 7. Summit and UFS observatories at the Mt. Zugspitze, Germany.

4   INSTRUMENTS DEPLOYMENT AND CAMPAIGN

During the FIRMOS campaign, measurements were performed using instruments deployed at both the Zugspitze Summit and at the UFS.

The spectrum of the DLR (downwelling longwave radiation) was measured in the FIR and mid-infrared spectral range from 100 to 3000 cm^{-1} (100–3.3 μm) using both FIRMOS, covering the 100-1000 cm^{-1} spectral range, and the E-AERI (Extended-range Atmospheric Emitted Radiance Interferometer), covering the 400-3000 cm^{-1} range.

FIRMOS was developed at CNR-INO with the support of ESA and installed in November 2018 on the terrace of the Summit. The instrument is a Fourier transform spectrometer (FTS) designed on the base of the heritage of a similar instrument, named REFIR-PAD (Radiation Explorer in the Far InfraRed – Prototype for Applications and Development), currently installed permanently in Antarctica. The FTS consists in an interferometric layout with double-input and double-output ports in Mach-Zehnder configuration, which increases the measurement reliability and the calibration precision. The instrument is able to cover the FIR radiation using wideband germanium-coated polyethylene terephthalate beam-splitters and room-temperature pyroelectric detectors. It was mounted within a plastic enclosure to protect optics and electronics for environmental such as snow when installed on the site, Figure 8.
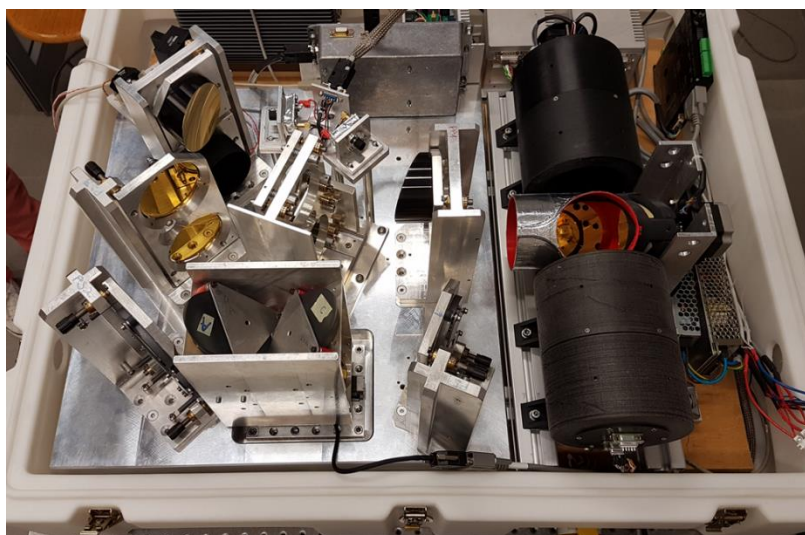

Figure 8. Optical and electronical components of FIRMOS inside the plastic enclosure.

E-AERI, manufactured by ABB Bomem Inc. (Quebec, Canada), routinely performs measurements from a permanent shelter on Summit (Sussmann et al., 2016), which is close to the FIRMOS installations, 4 m above the terrace, Figure 9. The Summit is served with standard PTHW (pressure, temperature, humidity, wind) meteo observations provided by the Deutscher Wetterdienst Deutschland. During the campaign, the instrument acquired 4987 spectra with 0.5 cm^{-1} of resolution. The measurement was performed every about 7 min when the weather conditions allowed the operations.
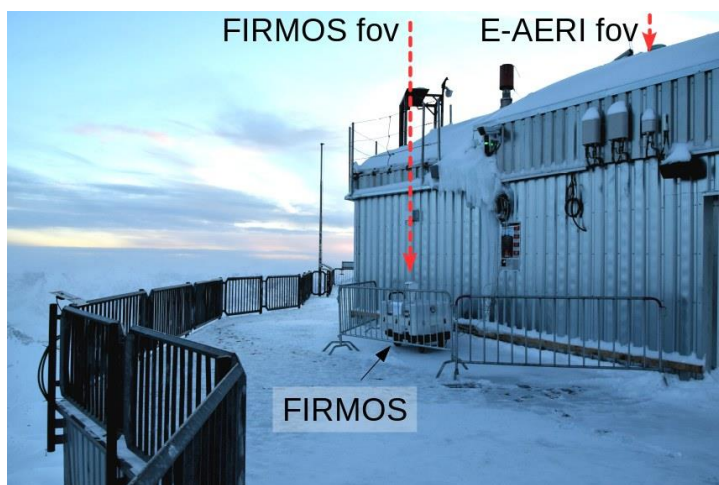
Figure 9. FIRMOS and E-AERI field-of-views (fov) on the terrace and the shelter on the Zugspitze Summit.

Two lidar systems were used to provide microphysical and geometrical information of cirrus clouds and additional vertical profiles of the water vapour mixing ratio and temperature. The lidar systems are located at the UFS observatory (Figure 10a).

Figure 10.a. Stratospheric aerosol lidar at UFS in action during the FIRMOS campaign.

Cirrus cloud properties are detected with the stratospheric aerosol lidar of KIT, which is a pure backscatter lidar operating at a wavelength of 532 nm. This system was operated in a semi-automatic mode, with a sequence of one profile each 4 or 10 minutes and an integration time of 1 min. The optical depth of cirrus layers was calculated with a Klett-type algorithm using different K-values between 0.67 and 1 and a direct method by directly analysing the extinction of the lidar signal (vertical shift of the signal after multiplying

with altitude r^2 and taking its logarithm). The two methods of retrieving lidar OD show a good agreement in most cases. We assume that cases with significant differences are assigned to variations of the size distribution and microphysical properties of the cirrus ice particles (Fig. 9b).
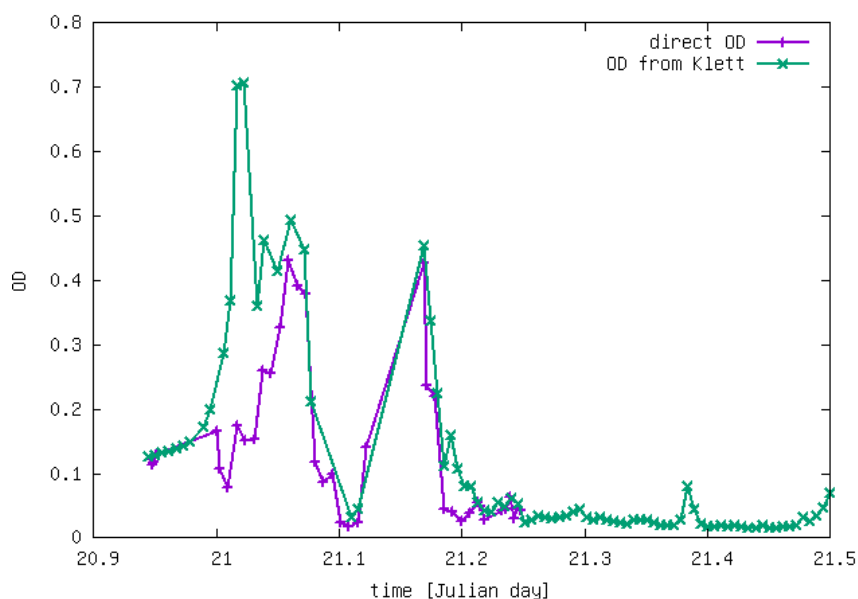

Figure 9b: Lidar ODs calculated with a Klett-type method (green) and calculated directly from the observed extinction (violet). The differences around noon on Feb 6, 2019 are tentatively assigned to variations in the microphysical properties of cirrus ice particles.

Water vapour and temperature profiles were performed alternatively with a Raman lidar system using a XeCl-Laser at 308 nm for the water vapour and with a Nd:YAG laser at 355 nm for the temperature. The latter measurements were carried out manually in order to switch between one laser to the other. Water vapour profiles were recorded with 1 million of laser shots, an integration time of 1 hour and a vertical resolution of 30 m near ground (4 km AMSL) and 250 m at 15 km AMSL. Temperature profiles were derived from density profiles measured only in absolute clear-sky conditions with an integration time of typically 1 hour and a vertical resolution of 30 m near ground (4 km AMSL) and 2 km at 80 km AMSL.

Atmospheric soundings with standard radiosondes are routinely available from the nearby stations of Munich airport, 100 km North the Summit, and Innsbruck airport 33 km South-East.

Specific balloon radiosoundings for cirrus cloud microphysics were performed on two days (5-6 February 2019) under clear sky and thin cirrus cloud conditions during night time. The antenna for communication with the balloon was build up on the Summit laboratory and the preparation of the sonde payload and launch took place at KIT IMK-IFU, Campus Alpin, in Garmisch-Partenkirchen (Lat. 47.476E, Lon. 11.062N, 730 m AMSL) about 8 km North-East of the Zugspitze. The balloon sondes are equipped with a standard radiosonde (Vaisala RS41-SGP), a CFH frostpoint hygrometer for measuring water vapour profiles with high accuracy, an ECC ozone sonde and the COBALD (Compact Optical Backscatter Aerosol Detector), developed in cooperation with the ETH Zürich, that provides extinction profile at two wavelengths (455nm and 870nm) and colour index within the cloud layers. The combined balloon payload is well tested and regularly also used by the GCOS Reference Upper Air Network (GRUAN) (e.g., Dirksen et al., 2014). The CFH has an uncertainty of about 2-3 % in the troposphere and less than 10 % in the lower stratosphere. Thus, the CFH is especially suitable

for measuring water vapour under the dry conditions at the tropopause and in the stratosphere up to altitudes of 28 km.
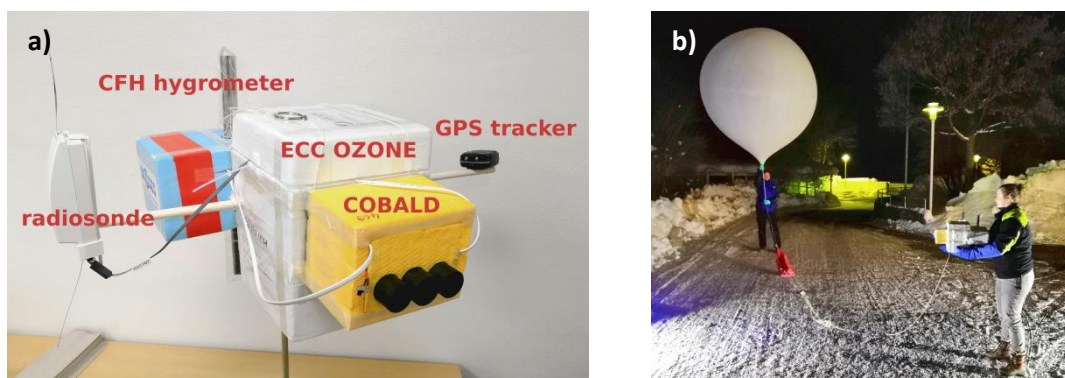

Figure 10. a) Balloon payload consisting of a radiosonde, CFH hygrometer, ECC ozone and COBALD instrument; b) Balloon launch at KIT Campus Alpin on the 06 February 2019.

The campaign took place from 29 November to 18 December 2018 and from 21 January to 20 February 2019. Measurements were performed when the weather conditions allowed the operations. This occurred for 33 days. The first part of the campaign in November-December 2018 was necessary to install the new instruments, try different deployment options, adjust acquisition parameters, and make some tests of operations. The weather conditions during that period were not very good and only a few days of clear sky occurred for testing instrumentation (only 43 sky observations). This first part is considered an engineering campaign for the deployment and preparation of the full suite of instruments. The data analysis shown in the following sections is limited to the second part of the campaign in 2019.

Table 3 reports the deployed instrumentation with the main measurement specifications and date.

Table 3. Instrumentation deployed at Zugspitze during the FIRMOS campaign.

Instrument	Location	Type of measurement	Integration time/repetition	Date
FIRMOS	Zugspitze Summit	DLR Spectrum 100-1000 cm^{-1}		
		Spectral res. = 0.4 cm^{-1}	128 s / 256 s	29/11/18 – 1812/18 1357 spectra
		Spectral res. = 0.3 cm^{-1}	210 s / 420 s	21/1/20 - 20/2/20 1477 spectra
E-AERI	Zugspitze Summit	DLR Spectrum 400-3000 cm^{-1} Spectral res. = 0.5 cm^{-1}	214 s / 440 s	28/11/18-20/2/19 4987 spectra
Meteo station	Zugspitze Summit	Local PTHW	10 min	Continuous
Backscatter lidar	UFS	Extinction profile	1 min / 4-10 min	16 Nov 2018 to 19 Feb 2019
Raman lidar	UFS	Water vapour and temperature profiles	1 h	16 Nov 2018 to 19 Feb 2019
Dedicated Radio-soundings	IMK-IFU, Garmisch-Partenkirchen	PTH profile, Ozone profile, cloud extinction and colour index profile		4 launches on 5 and 6 Feb under clear sky and thin cirrus cloud conditions during night time
Meteo service Radio-soundings	Muenchen-Oberschleissheim (Station No. 108689)	PTH profile	-	Daily at 00 and 12 UTC
Meteo service Radio-soundings	Innsbruck-Flughafen (Station No. 11120)	PTH profile	-	Daily at 03 UTC

5 CLEAR SKY ANALYSIS

The clear sky measurements of the 2018 and 2019 campaigns were analysed using the KLIMA ((Kyoto protocol and Informed Management of the Adaptation) simulation tools (available within the team) (Cortesi, et al., 2014). Here we report the results obtained from 2019 campaign only. The results obtained from the 2018 campaign are described in D7 and are not summarized here because they are not statistically significant (only 43 clear sky cases are found). After the delivery of the D7, further tests were made, in particular the forward model (spectroscopic database and continuum model) was updated and settings of the retrieval has been aligned with the SACR (Simultaneous Atmospheric and Cloud Retrieval) code (Di Natale, Palchetti, Bianchini, & Del Guasta, 2017) (Marquardt parameters and a-priori information – values and errors) used for the analysis of the cloud observations. In this section we report the last retrieval results obtained after the D7 deliverable. When the results described in D7 are still valid but not so substantial to be included in the final report, we will refer to it explicitly in this document.

The KLIMA algorithm comprises the FM (Forward Model) module and the RM (Retrieval Model). The FM is a line-by-line radiative transfer model, capable to simulate wideband spectral radiances from 100 to 1600 cm^{-1} (i.e. the FORUM spectral range requirement). The radiative transfer calculations are performed using Curtis–Godson approximation; the atmospheric line shapes are modelled with Voigt profile, the atmospheric continuum model takes into account the main contributions from N_2, O_2, O_3, H_2O, and CO_2. The spectroscopic database adopted for the simulations is AER version aer_v_3.7, the atmospheric continuum is modelled using the MT_CKD_3.3 routine considering the contribution of the lines external to the region of ± 25 cm^{-1} from the line centre. To account for the optical depth of the atmospheric layer at the different frequency a correction of the Planck function is included.

The RM uses a constrained NLSF (Nonlinear Least Square Fit) approach, the cost function to be minimized includes a priori information (optimal estimation method) and the Marquardt parameter. The exploitation of broadband measurements is made possible through a procedure that reduces the impact of systematic uncertainties. The code carries out a multi-target retrieval simultaneously retrieving more than one species, thus removing systematic errors due to interfering parameters. A complete VCM (Variance Covariance Matrix) can be used, including both the measurement errors and the errors in the calibration procedure and/or in the estimate of FM parameters.

The Level 2 analysis was carried out with the following retrieval configuration:

•   Retrieved targets: H_2O and Temperature profiles (multi-target retrieval)

•   Vertical retrieved profiles on 6 atmospheric levels

•   Initial Guess and a-priori values from the NCEP database

•   A-priori errors on Temperature = 0.3%

•   A-priori errors on H_2O = 50%

The DOF (degrees of freedom) for the clear sky retrievals were calculated from the trace of the averaging kernel matrix for each measurement giving values of 2.2-2.5 for temperature and 2.2 – 3.5 for water vapour.

5.1   A-POSTERIORI SPECTRAL CORRECTION: BIAS IN THE ATMOSPHERIC TRANSPARENT WINDOW AND FREQUENCY SHIFT

An a-posteriori evaluation of the calibration accuracy (bias and frequency shift) was achieved using the results a first Level 2 retrieval analysis on 2019 clear-sky observations (major details in D7).

This analysis was performed by studying the average retrieval residuals in clear-sky conditions (difference between simulated and observed spectrum). The results show values of the residuals higher than the average estimated calibration error CalErr in several regions of the spectrum (see Figure 11). In particular, a small bias of about 1–1.5 mW/(m^2 sr cm^{-1}) is observed in the spectral range from 750 to 1000 cm^{-1} in correspondence to the atmospheric transparent window. In this transparency window the clear sky model is deemed to be sufficiently accurate because the atmospheric contribution is very close to zero emission, therefore the high values in the residuals seem to be due to calibration errors present in the measured spectrum.
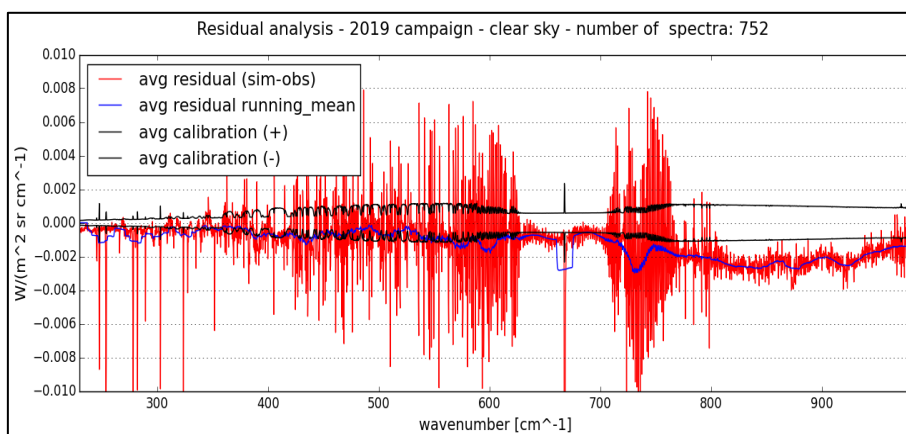

Figure 11. Averaged clear sky residuals (difference between simulated and observed spectrum). Red curve is the average residual; blue curve is a running mean on the average residual (the mean is executed on a spectral interval of 8 cm^{-1}); black curves are the CalErr.

Different solutions were studied finding that the problem is related to the strong phase error introduced by the very large flatness error of the beam-splitters that cannot be compensated by the phase-error correction of the Level 1 analysis. Since this error is constant, we decided to adopt a solution to compensate the bias in the transparent windows by applying an a-posteriori correction to the calibration in the spectral range 750–1000 cm^{-1} as shown in Figure 12. The spectrum in the range 100–750 cm^{-1} is left unchanged.
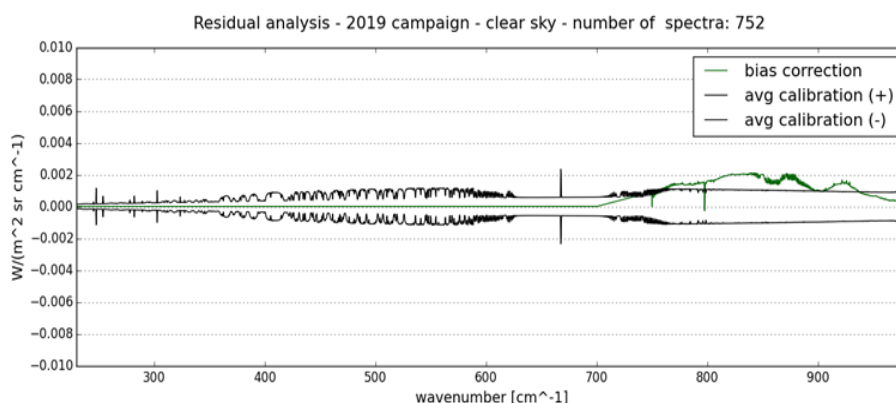
Figure 12. Average bias smoothed using a running mean on 8 cm^{-1} interval range (green curve) and calibration error (black curve). The average bias has been used for the a-posteriori correction of all the FIRMOS spectra.

The comparison of measured and simulated average spectrum (residuals) shows also a small frequency shift of about +50 ppm between simulations and observations ($\sigma_{real} = \sigma_{firmos} + 5\ 10^{-5}\ \sigma_{firmos}$). Figure 13 shows the difference between simulated and observed spectra in clear sky condition. When a frequency-shift of 50 ppm is applied to the measured spectra, the residuals are significantly reduced in all the range (with exception of the bias in the 650–1000 cm^{-1} window), Figure 13.

FIRMOS Level 1 dataset is not corrected for the frequency-shift, the information is provided as a shift of the peak of the ISRF (Instrumental spectral response function) to be used for further analysis such as the retrieval.
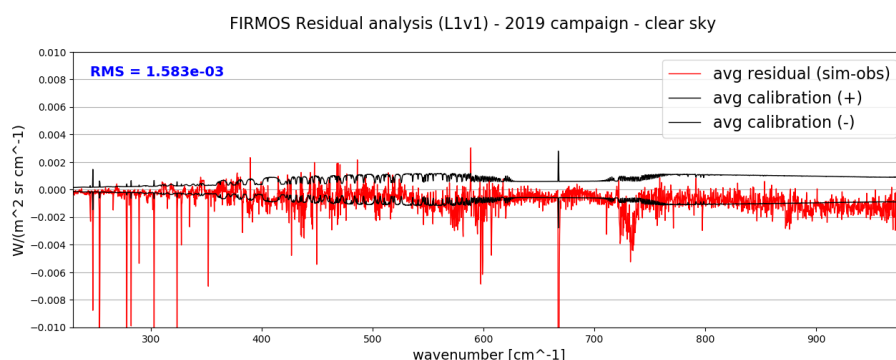

Figure 13. Mean residuals after bias and frequency shift correction.

5.2   COMPARISON WITH E-AERI MEASUREMENT

A comparison with E-AERI was performed in order to qualify FIRMOS measurements with a standard commercial spectrometer. Only measurements acquired within a 10-minutes of temporal distance were considered coincident and selected to calculate the average spectrum. In Figure 14 the two average spectra for the 2019 campaign are contrasted. For this comparison FIRMOS and E-AERI spectra are resampled at the common spectral resolution of 0.5 cm^{-1} by applying the same apodization function (Norton-Beer strong). We found that also E-AERI measurements were affected by a frequency shift of the wavenumber scale of -50 ppm ($\sigma_{real} = \sigma_{E\text{-}AERI} - 5\ 10^{-5}\ \sigma_{E\text{-}AERI}$), as in FIRMOS; but with different sign. The frequency scale was therefore

recalibrated with this correction before the comparison. A good agreement between the two instruments is found in the common spectral range from 400 to 1000 cm^{-1} with the difference that is within the NESR estimate, a part a few points where strong water vapour and CO_2 lines are present, caused by the different location of the two instruments, and the feature of the beam-splitter absorption around 730 cm^{-1}.
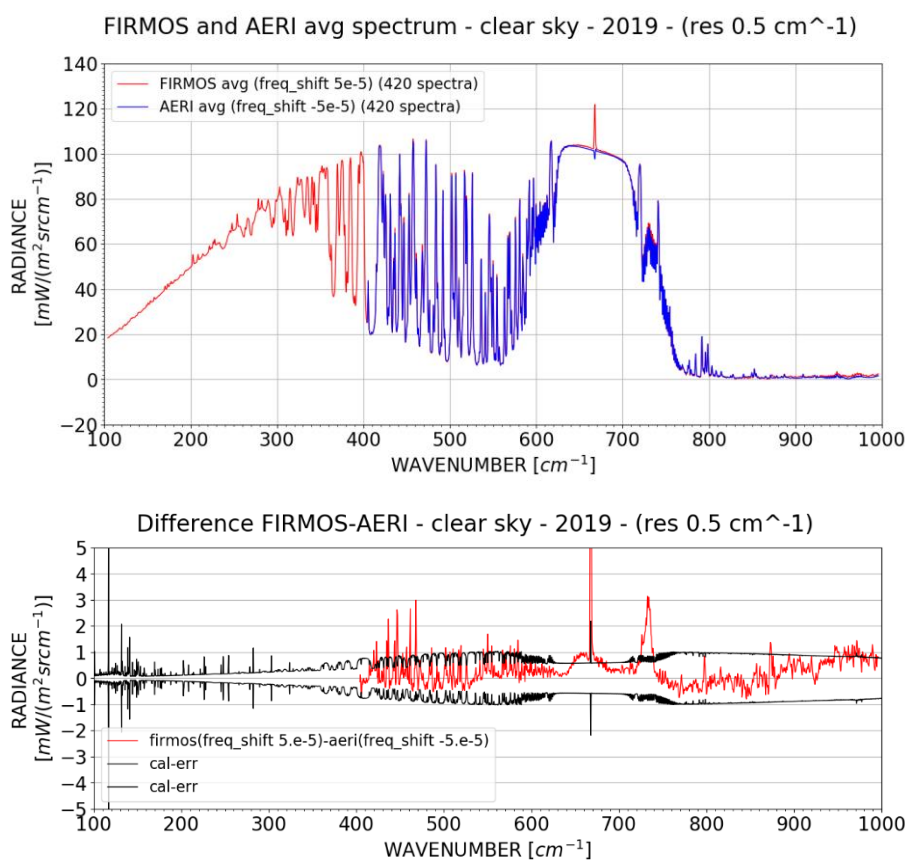

Figure 14. Comparison between FIRMOS and E-AERI spectra for the 2019 campaign. Spectra were resampled to a common spectral resolution of 0.5 cm^{-1}. The top graph shows FIRMOS (red) and E-AERI (blue) average spectra. The bottom graph shows the difference between the average spectra (in red), compared with the calibration error (in black). The blue curve is a running mean on the average residual executed on a spectral interval of 8 cm^{-1}.

5.3 CLEAR SKY SELECTION

Clear sky selection was needed to retrieve the atmospheric profiles with the KLIMA code. Moreover, the clear sky selection was useful to identify calibration problems because, without cloud, the spectrum in the atmospheric window is well known and very close to zero. The clear selection has to identify which measurements can be analysed by KLIMA that are: the clear sky scenes and the cloudy sky scenes with very optically thin clouds, so that, the spectrum is not significantly perturbed by the cloud in the FIRMOS band.

Clear sky cases were selected by evaluating the transparency and the slope of the FIRMOS spectra in the atmospheric window. The criterion was set up by using clear and cloudy scenes selected with the lidar backscattering profiles, in the period between 21st January 2019 and 07th February 2019. The lidar profiles

were interpolated in the time domain with the FIRMOS measurements, obtaining a single lidar profile for each FIRMOS spectrum, which was then flagged as clear and cloud by means of a routine, developed specifically for this purpose. This routine fits in 8 different altitude ranges between the ground and 20 km the lidar signal with an exponential law. The relative differences Δ between the signal and the model are then exploited to select the cases. When the maximum of the sum of relative differences Δ in the 8 ranges is greater than 0.5 the scene is flagged as cloudy otherwise as clear sky, Figure 15.
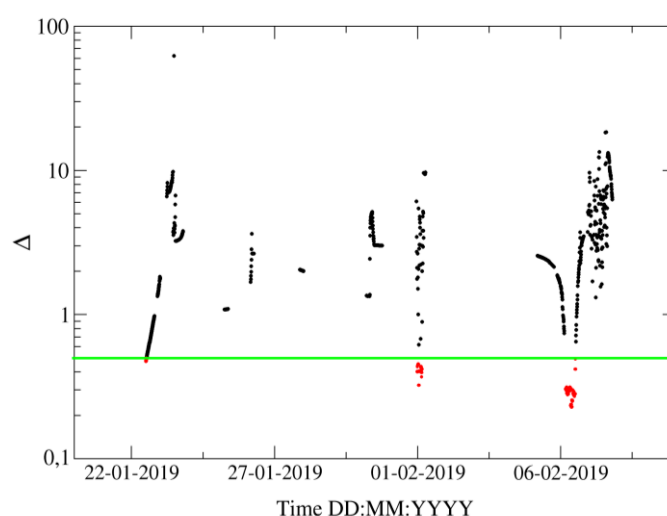

Figure 15. Relative differences Δ between the signal and the model calculated for clear sky (red) and cloud (black) conditions.

This method allowed to get two distinct datasets related to the clear and cloudy scenes using only the lidar information. Then, for each corresponding FIRMOS measurement, the value of the transparency in the band 829-839 cm^{-1} and of the slope in the band 750-980 cm^{-1} were evaluated. The scatter plot of the transparency vs the slope for each dataset is shown in Figure 16, red dots for clear sky and black dots for cloudy. The plot allowed to infer the thresholds for discriminating the clear sky scenes. From Figure 16, we can see that all the clear sky scenes (in red) have slope values below 5.7×10^{-5} W/(m^2 sr cm^1)/cm^1 and transparency below 0.011 W/(m^2 sr cm^1). In the same ranges we can see (in black) the presence of very optically thin clouds in the far infrared.
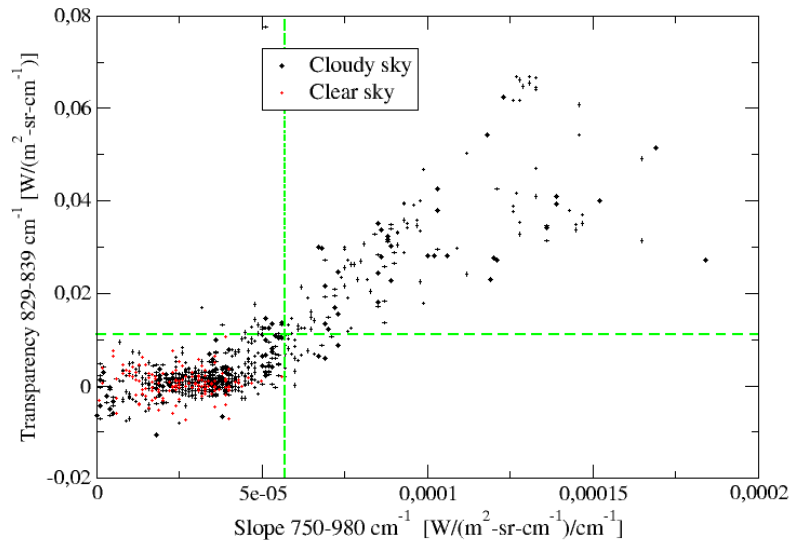
Figure 16. Scatter-plot of the slope in the [750-980] cm^{-1} and the mean radiance of the spectra in channel [828-839] cm^{-1}.

Summarizing: if both measurements have an offset (in 828-839 cm^1) < 0.011 W/(m^2 sr cm^1) and a slope (in 750-980 cm^1 < 0.000057 [W/(m^2 sr cm^1)/cm^1] then we consider the conditions to be clear.

5.4 χ^2 AND RESIDUALS ANALYSIS

The retrieval is performed on the whole clear sky Level 1 dataset minimizing the $\chi2$ of the fitting procedure. The following Figure 17 and Figure 18 show the $\chi2$ is close to 1 (with the exception of a few cases) demonstrating the good performances of the fitting procedure. Based on these results, the cases with χ^2 larger than 1.2 were excluded from the statistical analysis of the Level 2 products.
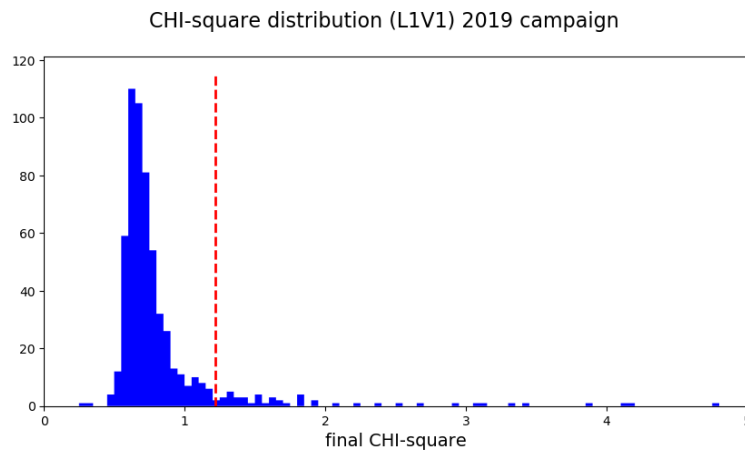

Figure 17. χ^2 distribution for 2019 campaign. Clear sky Bright skynts with χ^2 larger than 1.2 were excluded from the subsequent analysis.
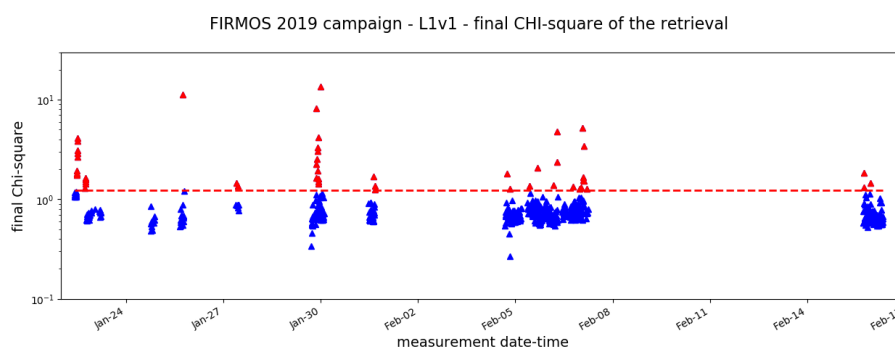
Figure 18. Complete plotting of the χ^2 of the fitting procedure on 2019 campaign. In red the χ^2 larger than 1.2.

A statistical analysis of the residuals was also checked against the estimation of the measurement NESR. The comparison between the standard deviation of the residuals and the NESR, shown in Figure 19, provides a
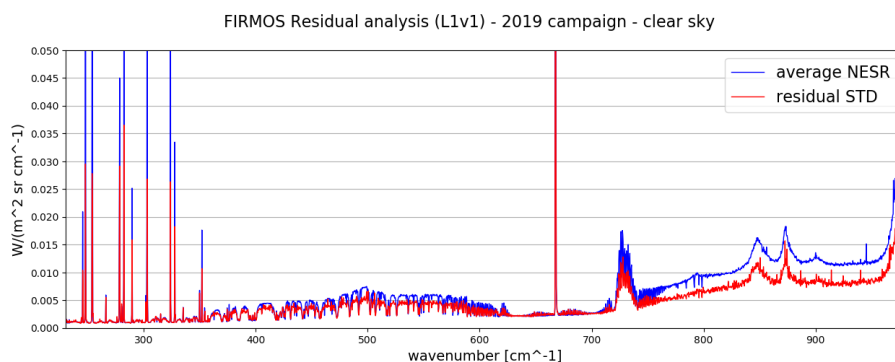

Figure 19. Compa. on between the standard deviation of residuals and the NESR.

5.5   RADIOSONDE VALIDATION OF WATER VAPOUR PROFILES

The Level 2 retrieval products for clear sky cases are the vertical profiles of H_2O and Temperature. The quality of the retrievals was evaluated by comparison with the closest and concomitant radio soundings, which was performed during the 2019 campaign with the launch of 4 dedicated radiosondes from KIT in Garmisch-Partenkirchen. The results of comparison of the retrieved profiles of H_2O with the radiosonde profiles are shown in Figure 20. The radiosonde profiles have a fine vertical resolution; therefore, they were convolved with the FIRMOS averaging kernels to compare them with FIRMOS Level 2 products. Figure 20 shows the average difference between all the FIRMOS H_2O profiles, retrieved from measurements near the radiosonde launch times, and the 4 radiosondes. The figure shows that the average difference falls inside the retrieval error range, validating in this way the FIRMOS H_2O retrievals.
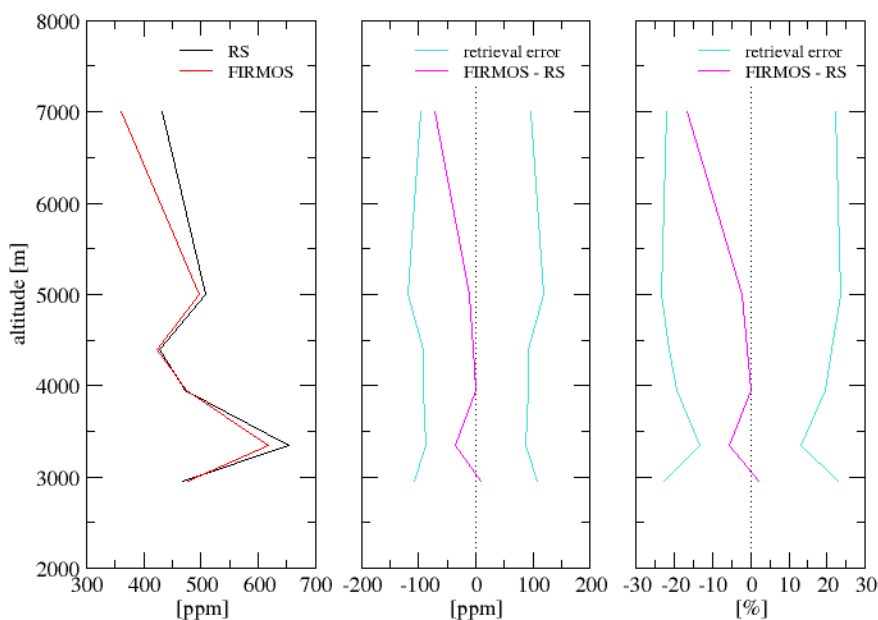
Figure 20. Comparison between FIRMOS Level 2 water vapour product and radiosonde profiles. The left-hand panel shows the average radiosonde profile in red and the average coincident FIRMOS profile in black. The other two panels show the average difference (curve in magenta, FIRMOS minus radiosonde profiles) in relation to the average FIRMOS retrieval error (cyan curves) in ppm (central panel) and in % (right panel).

5.6 INTEGRATED WATER VAPOUR VALIDATION

The IWV has been validated using the KIT algorithm for the retrieval of this parameter applied to both the FIRMOS and E-AERI datasets: IWV is retrieved by minimizing E-AERI (or FIRMOS) vs. LBLRTM (Line-By-Line Radiative Transfer Model) spectral residuals in the spectral range from 400 cm^{-1} to 600 cm^{-1}, see (Sussmann et al. 2016) for details.

Precision. The dominant contribution to IWV precision error is retrieval noise: The higher uncertainty value for FIRMOS precision (0.027 mm) compared to E-AERI (0.020 mm) is related to the higher spectral radiance noise of FIRMOS compared to E-AERI:

- Noise (E-AERI) = 0.50 mW / (m² sr cm^{-1})

- Noise (FIRMOS) = 2.26 mW / (m² sr cm^{-1})

Note that the lower noise in E-AERI spectra may be explained by the E-AERI using a cooled detector (67 K) while the FIRMOS uses a room temperature detector.

Accuracy. H_2O continuum and line parameters used in the forward calculation as well as a priori assumptions on the shape of the H_2O profile (NCEP), are factors impacting the accuracy of the IWV retrieval; however, they are common to E-AERI and FIRMOS retrievals and can therefore be disregarded for the IWV inter-comparison. Other factors are specific to the instruments and can cause biases between E-AERI and FIRMOS:

- altitude difference of 4 m between E-AERI and FIRMOS location

- frequency shifts in either or both E-AERI or FIRMOS spectra

- calibration errors

The impact of the altitude difference (E-AERI 2961 m AMSL, FIRMOS 2957 m AMSL) on IWV (FIRMOS-AERI) has been corrected by calculating IWV(2961 m) and IWV(2958 m) from the NCEP profile used as retrieval prior. The resulting difference used for altitude correction is 0.004 mm for the mean atmospheric state of the campaign, and the error introduced by this altitude correction should therefore be <<0.004 mm.

FTIR measurements can show small errors in the frequency scale due to tiny drifts of the calibration laser. Such frequency errors can propagate to IWV errors in the retrieval process because the measured spectrum is fitted to a theoretical spectrum, which leads to artificial spectral residuals than can be mis-interpreted in terms of IWV. Indeed, direct comparison of coincident FIRMOS and E-AERI spectra (Δt < 4 min) showed evidence for a small discrepancy in frequency scales. Therefore, we implemented to our IWV retrieval a joint fit of a frequency scale factor = 1 + frequency shift. The results are displayed in Fig. 19a and show a mean wavenumber scale factor of 1.0000555 for FIRMOS and 0.9999513 for E-AERI.
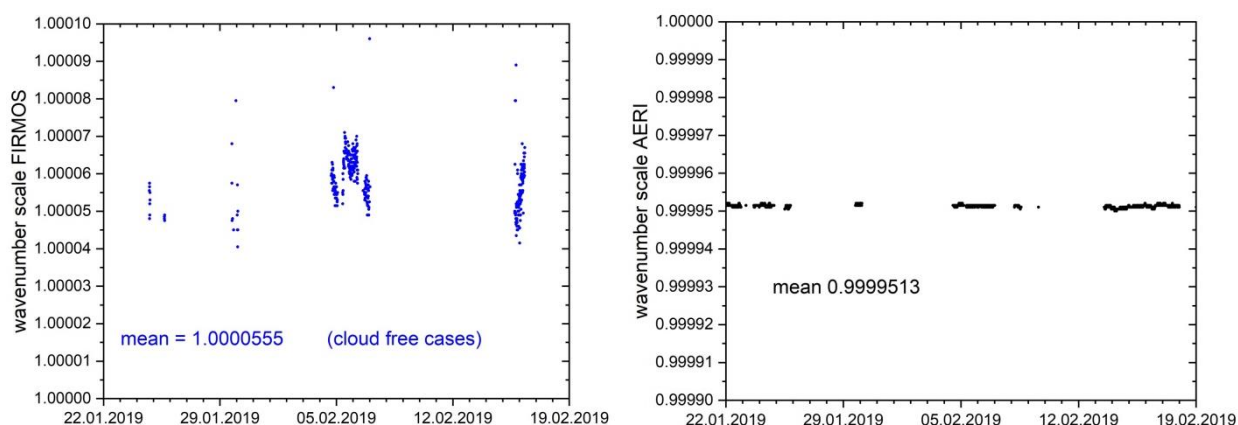

Figure 19a. Time series of frequency scale factors derived from a joint spectral fit during IWV retrieval. Left: FIRMOS, right: E-AERI.
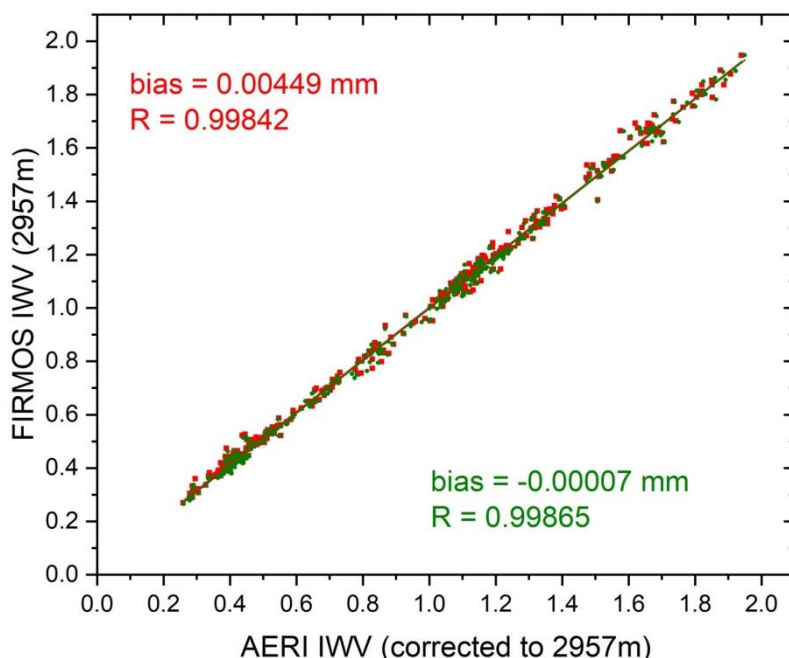
Figure 21b. Scatterplot of IWV values calculated for the two instruments. Red: IWV retrieval from AERI spectra and FIRMOS V1 spectra with frequency scale as is. Green: IWV retrieval from AERI and FIRMOS including a joint fit of frequency scale factors (for both instruments independently).

The impact from this joint frequency scale retrieval on IWV is shown in Fig. 19b. The IWV retrievals with the original spectra are displayed in red and there is a bias of ΔIWV(FIRMOS-AERI) = 00449 mm. For the IWV retrievals with joint frequency scale fit (green) the bias is practically eliminated to ΔIWV(FIRMOS-AERI) = -00007 mm. This bias of -0.0007 mm is negligible compared to the level of measured atmospheric IWV states ($\approx$0.2 – 2 mm, see Fig. 19b); i.e., there are no indications of significant calibration errors in the spectral domain of the H_2O rotational band.

5.7 TIME SERIES

Where the measurement sessions are sufficiently dense, the H_2O Level 2 retrieval results can be visualised as time series as in Figure 22. They could then be contrasted to ERA5 reanalysis data after a degradation of the FIRMOS products time resolution (i.e. averaging in time-bins of 1 hour comparable to ERA5 data). The FIRMOS time series (Figure 23) have some variability in comparison to ERA5 reanalysis (Figure 24) both on the altitude axis and along the time dimension, probably due to local weather conditions that cannot be represented in ERA5 nevertheless, the two-time evolutions are similar, recognising the increase in humidity at lower altitudes towards the early hours of 23 January.

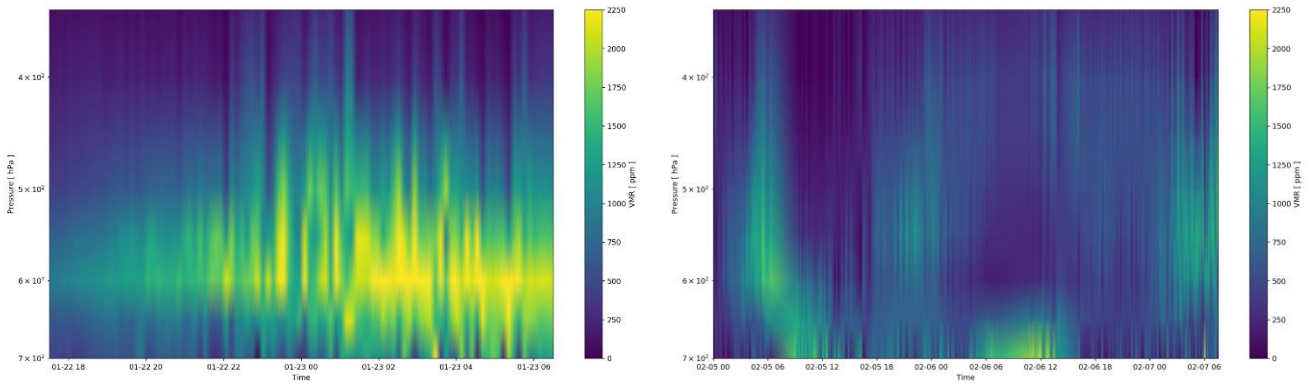| D8 "Final Report" | Doc. name: FIRMOS D8 final report |
ESA Contract No. 4000123691/18/NL/LF	Rev.: v3.6 - final
	Date: 10 April 2020
	Page: 28/48

Figure 22. Time series of FIRMOS Level 2 products mapping water vapour profiles retrieved from the set of measurement taken between 6.00 pm on 22 January and 6.00 am on 23 January 2019 (on left) and between 0.00 am on 5 February and 6.00 am on 7 February 2019 (on right). The time frequency is about 10 measurements per hour.
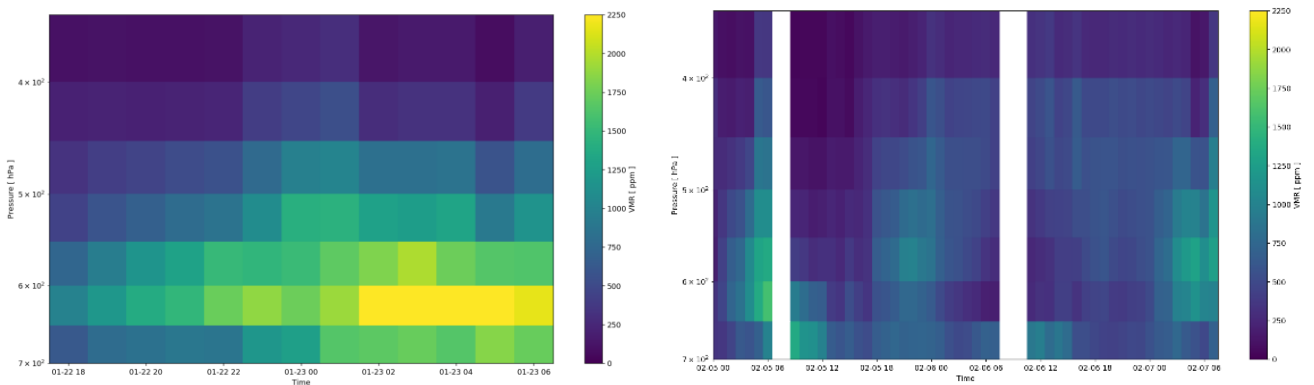

Figure 23. Time series of FIRMOS water vapour profiles, as in Figure degraded to ERA5 time resolution of one profile per hour.
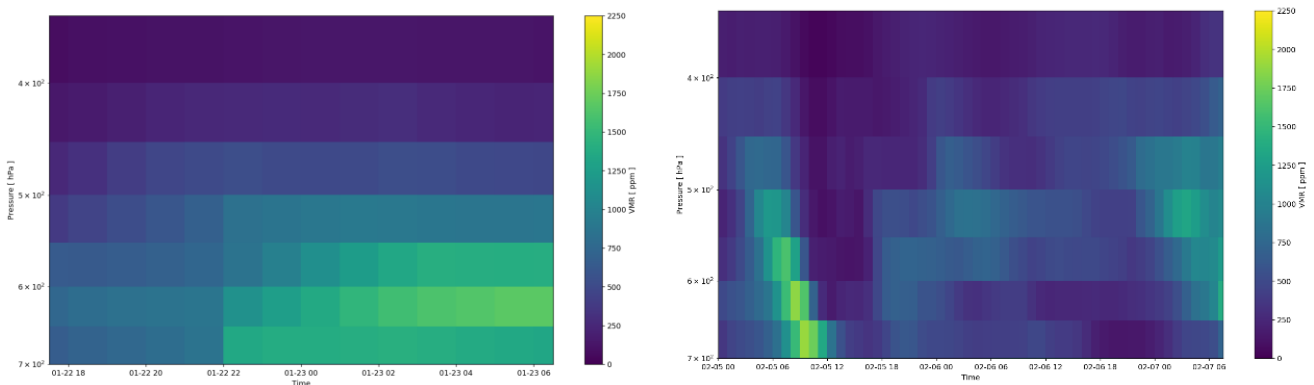

Figure 24. ERA5 water vapour time series for the pixel closest to Zugspitze.

6 CLOUDY SKY ANALYSIS

For the cloudy sky analysis, the SACR retrieval code (Di Natale, Palchetti, Bianchini, & Del Guasta, 2017) is used adopting cloud particle models with bullet rosettes habit (Yang, et al., 2013). The products are:

- Water vapour and Temperature profiles, retrieved at the same levels as KLIMA, along with ISRF broadening (mixing coefficient of sinc/sinc^2) and frequency scale factor;
- Ice fraction and water droplets sizes, De (ice particle equivalent diameter), OD (Optical Depth of ice), cloud bottom height

Figure 25 shows an example of a fitted spectrum compared with a corresponding measurement. The residual difference is always within the measurement uncertainty, demonstrating a good convergence of the retrieval algorithm.
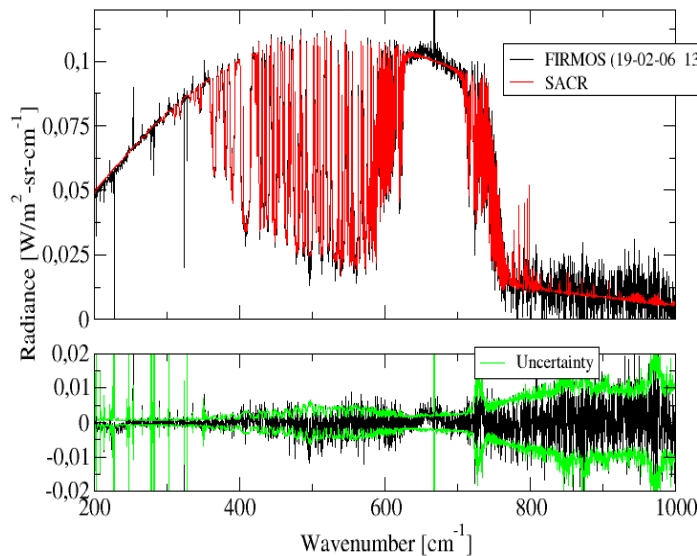

Figure 25. Example of measured spectrum compared with the fitted one. The bottom panel shows the residual differences compared with the measured uncertainty.

The frequency shift and the self-apodization coefficients have been fitted during the atmospheric and cloud retrievals assuming an ISRF which approximates the effect of self-apodisation due to the interferometer beam aperture Ω

$$ISRF(\sigma) = \alpha \, sinc(\sigma) + (1 - \alpha) \, sinc^2(\sigma)$$

with

$$\alpha = \, sinc\left(\frac{\Omega \sigma MPD}{2}\right)$$

where MPD is the maximum optical path difference. The retrieval procedure gives an average value of 55 ppm for the frequency shift, which corresponds to what was found previously, and 0.0012 for the self-apodization coefficient Ω.

The DOFs for the cloud parameters retrieval were calculated from the trace of the averaging kernel matrix for each measurement. The average value is of 4 DOFs out of 5 retrieved parameters (Ice fraction and water droplets sizes, De, OD, cloud bottom height). In case the lidar measurements were available, the lidar signal was used in coincidence of FIRMOS measurements to fix the cloud top and bottom and to weight the optical depth over a vertical grid with a resolution of 0.2 km between the top and the bottom. In all other cases the cloud bottom was fitted, assuming a single cloud layer of 1 km, together with the other cloud parameters and the atmospheric profiles.

In Figure 26 the retrieved cirrus parameters are shown and compared for the day 6 February 2019 with the analogous parameters obtained from the collocated and simultaneous measurements of the backscatter lidar. The OD values have been retrieved from the difference to the extrapolated signal below the cirrus layer (manually) and using the Klett's method (Klett et al., 1981). The Klett's method has been used in order to automatize the routine and extend the ODs calculation over the all measurements. The Klett method assumes the power law relationship between the cloud backscattering and the cloud extinction, in which the Backscatter-Extinction Coefficient Ratio K exponent is considered ranging between 0.67 and 1 for clouds, and it mainly depends on the cloud homogeneity. K is expected to be 1 in case of homogeneous layers and can be as low as 0.67 in inhomogeneous clouds.

The good agreement between ODs, shown by Figure 26, catching the variations occurred around midday, demonstrates the capability to retrieve cirrus parameters with passive measurements, such as the ones performed with FIRMOS.
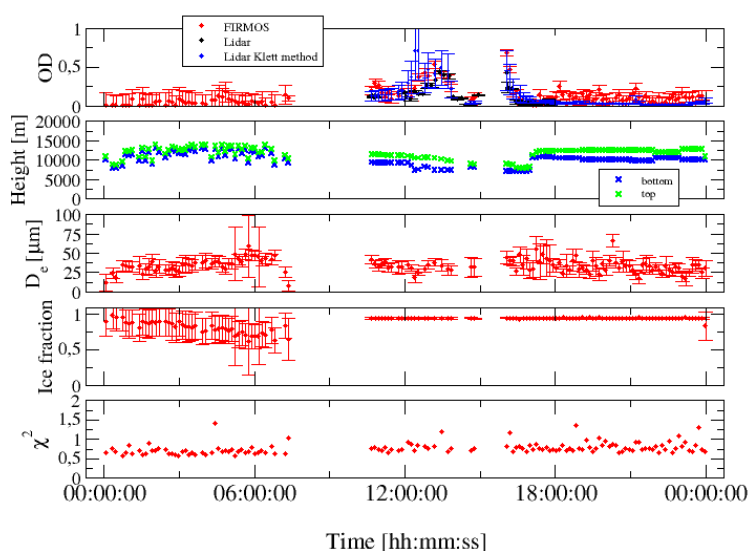

Figure 26. Cirrus cloud parameters for 06/02/2019 and comparison with lidar measurements (dots without error bars).

An example of the retrieved cloud parameters for the 2019 campaign during the day 30 January is also shown in Figure 27, in which we can see the passage from a high thin ice cloud, at 8-10 km of height, to a low thick water cloud, very close to the ground. In this case the bottom has been fitted assuming a geometrical thickness of 1 km, since no lidar measurements were available for that day. Furthermore, the figure shows the optical depth of liquid water (OD_w) derived from the retrieved ice fraction, De and water droplets size.
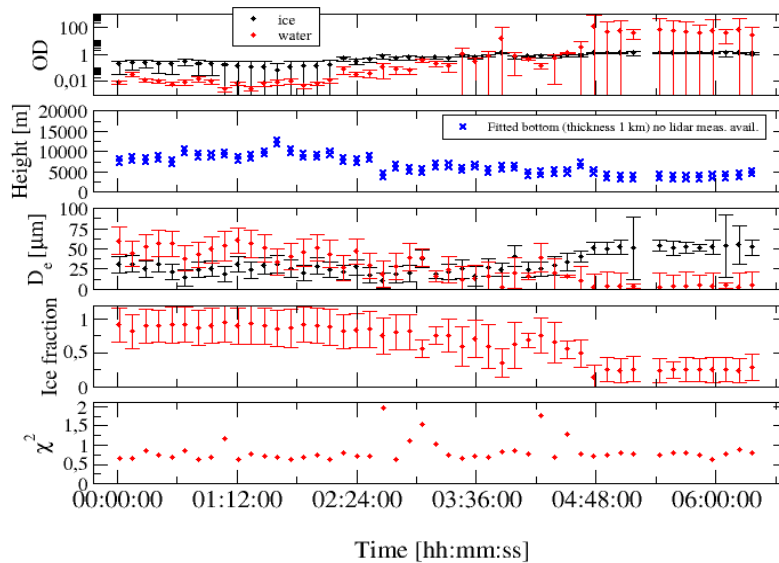

Figure 27. Cloud parameters for 30 Jan. 2019, from a high cirrus cloud to a low a thick water cloud.

In Figure 28 we show the cloud parameters for all the measurements performed in January and February 2019, as a function of the total optical depth $OD_{tot} = OD + OD_w$. IWP (Ice Water Path) and LWP (Liquid Water Path) are derived from the other cloud retrieved parameters.
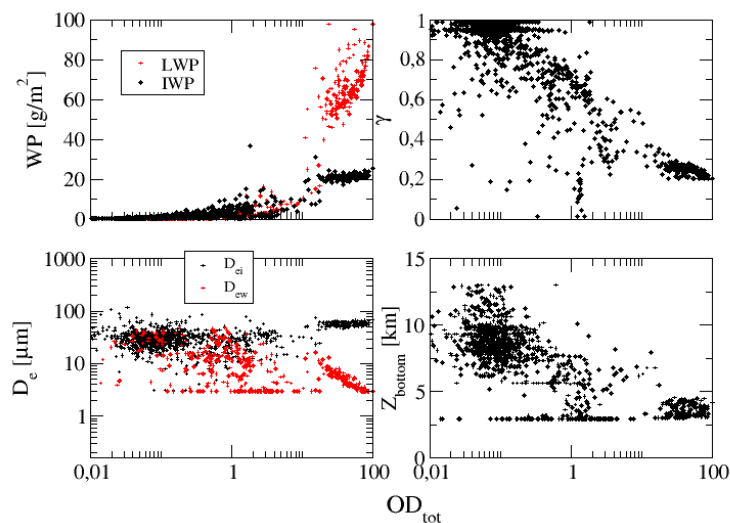

Figure 28. Cloud parameters as a function of the total optical depth for the whole campaign among January and February 2019. From the left top up to the right bottom we find the water path of ice and water (black and red), the ice fraction, the effective diameter

Finally, in Figure 29 the scatter plot for the OD retrieved from FIRMOS and from lidar measurements with the Klett method is shown using different values of K. K. values of K give a better agreement with the FIRMOS measurements giving the indication that we are observing a non-homogeneous cloud layer.
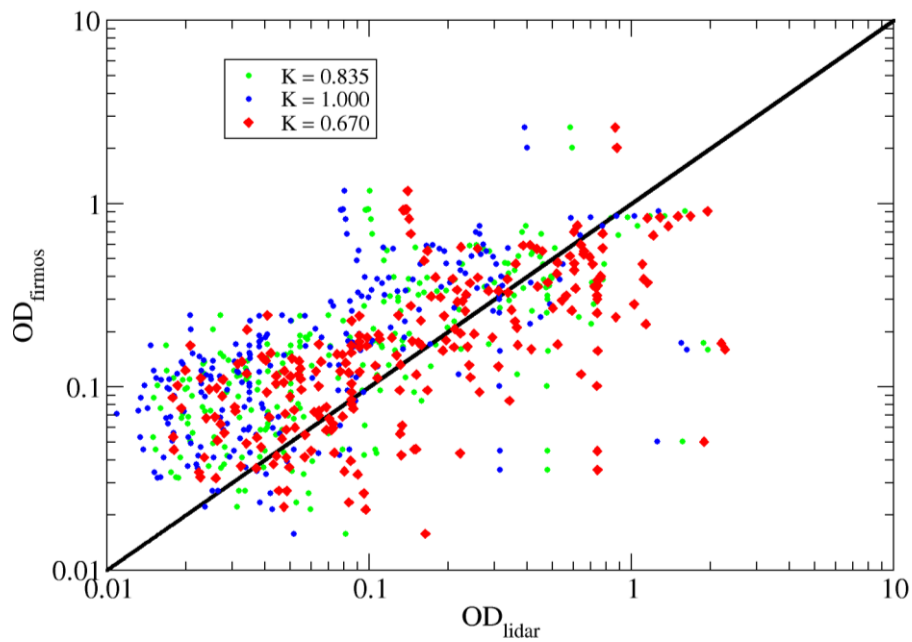

Figure 29. Scatter plot for the whole FIRMOS campaign between the optical depths (ODs) retrieved from FIRMOS and lidar measurements. The three different colours denote different values of the Backscatter-Extinction Coefficient Ratio K used in the Klett's method for the lidar calculation.

7 FAR-IR SPECTRAL CHARACTERISATION OF SNOW EMISSIVITY

The four days at the end of the second Zugspitze campaign were devoted to measurements of snow samples with the objective to characterise the spectral emissivity of snow measuring the spectrum of the radiance emitted by the surface.

Snow measurements were carried out on the 18th and 19th February 2019, after test sessions on the two previous days.

FIRMOS was adapted to observe at nadir, the instruments parameters (resolution, spectral range, acquisition time) were not modified.

Figure 30 FIRMOS during snow test measurements. The bright red spot in the centre of the FOV is due to the alignment laser

The instrument was tilted to distance the observed point from FIRMOS, in this way the samples were homogeneously illuminated by the sky. In this way the main contributions to the measured radiance are by the surface emission and by the sky reflection.

The snow samples were placed under the instrument FOV at about 90 cm from the input mirror. The beam size on the snow was about 8-9 cm in diameter depending on the distance and inclination. The tilt angle was 13.5° the maximum possible for the instrument operations.

To attain diversity in the snow type, 10 samples were collected in the vicinity of the Zugspitze summit and close to Zugspitzplatt station, on the 18th and 19th February 2019. Each sample was measured by FIRMOS for roughly 90 minutes, and successively characterized in terms of type, density, and Specific Surface Area (SSA).

Table 4 lists the experiments carried out during the 18th and 19th February.

Table 4 List of the experiments made on 18th and 19th February.

Sample name	Description	id	Number of spectra
ICE	Ice	20190218-1751	10
FS	Fresh snow	20190218-1938	12
ACC30	Accumulated 30cm snow	20190218-2136	11
DH	Depth hoar snow	20190219-0644	13
DHRUG	Depth hoar snow with grooves	20190219-0901	12
RGREF	Melted forms snow	20190219-1052	7
MFREF	Refrozen snow - natural case	20190219-1300	14
DS	Dense slab snow	20190219-1631	14
ACC100	Accumulated (100 cm) snow	20190219-1848	13
ACC70	Accumulated (70 cm) snow	20190219-2100	12

7.1   SNOW CHARACTERIZATION

Snow was characterized by type, density, SSA (Specific Surface Area), and details on the experimental conditions.

SSA [m^2 kg^{-1}] is the Area of Air/Ice interface per kilogram of snow, characterizing the ratio between scattering and absorption properties of the snow sample. It is also a proxy for snow grain size assuming spherical shapes. SSA ranges from 100-150 m^2 kg^{-1} for very fresh dendritic snow (fine snow) to 5-10 m^2 kg^{-1} for coarse old snow, it was retrieved by means of a DUFISSS (DUal Frequency Integrating Sphere for Snow SSA) sensor measuring snow reflectance at 1310 nm.

Density [kg m^{-3}] ranges from 25-50 kg m^{-3} for very fresh light snow to 600-800 kg m^{-3} for old snow/firn.

Figure 31 shows the samples collected had a good diversity in in terms of SSA and Density. Moreover, the natural range of possible values for these parameters is well explored (except very fresh/light snow and dense old snow). Note that ICE is represented with a grey symbol since its SSA and Density were prescribed

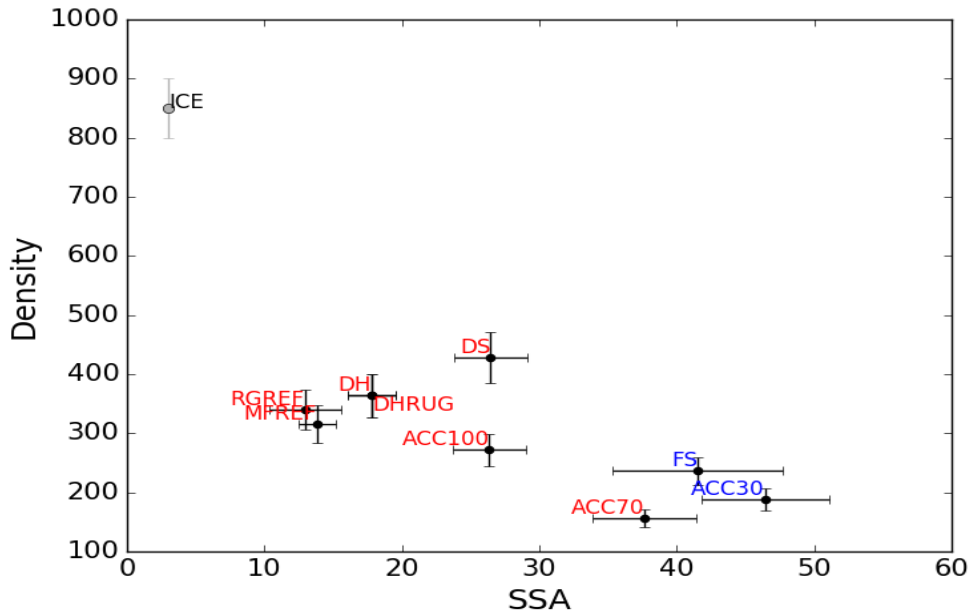and not measured. Values of SSA=3 m² kg⁻¹ and density of 850 kg m⁻³ were prescribed on the graph as typical values in literature.

Figure 31. SSA (m² kg⁻¹) as a function of Density (kgm⁻³) for the different samples. ICE sample label is in black, snow samples of February 18th in blue, and those of February 19th in red.

7.2   EMISSIVITY RETRIEVAL METHOD

The retrieval method is a simplified version of the one proposed in (Bellisario, et al., 2017), as the ground is assumed to reflect as a specular surface (in the journal paper the authors assume a Lambertian surface but they note that replacing this assumption with that of specular surface has very little impact on the final emissivity values they retrieve).

In this context the surface upwelling nadir radiance $L^{\uparrow}_{v,surf}$ is:

$$L^{\uparrow}_{v,surf} = \epsilon_v B_v(T_s) + (1 - \epsilon_v) L^{\downarrow}_{v,surf} \tag{1}$$

ϵ_v is the spectral emissivity (the target variable), $B_v(T_s)$ the Planck emission at the surface temperature T_s and $L^{\downarrow}_{v,surf}$ the downwelling zenith radiance. The two radiance terms in Equation 1, $L^{\uparrow}_{v,surf}$ and $L^{\downarrow}_{v,surf}$ are related to FIRMOS measurements through Equations 2 and 3:

$$L^{\uparrow}_{v,FIRMOS} = \tau_v L^{\uparrow}_{v,surf} + \tau_v E^{\uparrow}_v \tag{2}$$

$$L^{\downarrow}_{v,surf} = \tau_v L^{\downarrow}_{v,FIRMOS} + E^{\downarrow}_v \tag{3}$$

Where $L_{v,FIRMOS}^{\uparrow}$ and $L_{v,FIRMOS}^{\downarrow}$ are the radiances measured looking at the snow sample and at the sky, respectively, $E_v^{\uparrow}$ and $E_v^{\downarrow}$ are the upwelling and downwelling emissions of the atmospheric layer between FIRMOS and the surface, τ_v is the transmission of such layer.

Finally, combining previous equations, the spectral emissivity ε_v is calculated as:

$$\epsilon_v = \frac{L_{v,FIRMOS}^{\uparrow} - \tau_v^2 L_{v,FIRMOS}^{\downarrow} - \tau_v E_v^{\downarrow} - E_v^{\uparrow}}{\tau_v(B_v(T_s) - \tau_v L_{v,FIRMOS}^{\downarrow} - E_v^{\downarrow})} \tag{4}$$

The emission terms and the transmission are calculated by means of the HITRAN Application Programming Interface (HAPI) (Kochanov, et al., 2016) using as input air temperature and humidity data from the Zugspitze weather station by the DWD – CDC (Deutscher Wetterdienst Climate Data Center).

The surface temperature Ts is retrieved from FIRMOS measurements in the atmospheric window spectral interval 940÷960 cm-1.

In (Bellisario, et al., 2017) the authors apply Equation 4 to the Tropospheric Airborne Fourier Transform Spectrometer (TAFTS); a TAFTS observation sequence includes nadir and zenith views (measuring upwelling and downwelling radiances, respectively). That is not possible with FIRMOS, as during the campaign it alternated relatively long sky views (nadir −13.5°) to various snow views (zenith +13.5°); see Table 5 as an example of the measurement schedule for 18th February.

In the case of the FIRMOS measurements, each snow/ice sample session was coupled with the sky viewing session nearest in time. Moreover, to reduce the noise, the average of all the spectra of each sample was substituted to $L_{v,FIRMOS}^{\uparrow}$ in Equation 4. In the same way downwelling radiance spectra were averaged ($L_{v,FIRMOS}^{\downarrow}$ in Equation 4), in the case of long sequences (e.g. the 2nd sky view in Table 5) the spectra measured in the one and half hour nearest to the snow measurement were averaged, in order to deal in Equation 4, with radiances from roughly the same number of spectra.

Table 5 Measurement schedule 18th February 2019.

Measurement	Start time	End Time	
Sky view	16:30	17:30	Clear sky (sunset 17:44)
Ice	17:51	19:07	Ice sample
FS	19:38	21:10	Fresh snow sample
ACC30	21:36	23:00	Accumulated 30 cm snow
Sky view	23:38	06:19 (19th February)	Clear sky

The resulting raw emissivity is very noisy and contains some unphysical outliers, for this reason the data is filtered discarding the values corresponding to transmission values lower than 0.9 again following the procedure in (Bellisario, et al., 2017). Spectral emissivity is a smooth function therefore the (still noisy) filtered values are successively averaged on spectral intervals 25cm^{-1} wide. The values around the CO_2 667 cm^{-1} band and in the 300-350 cm^{-1} range are still often noisy due to the high sensitivity to the surface temperature and to the absorption of the signal.

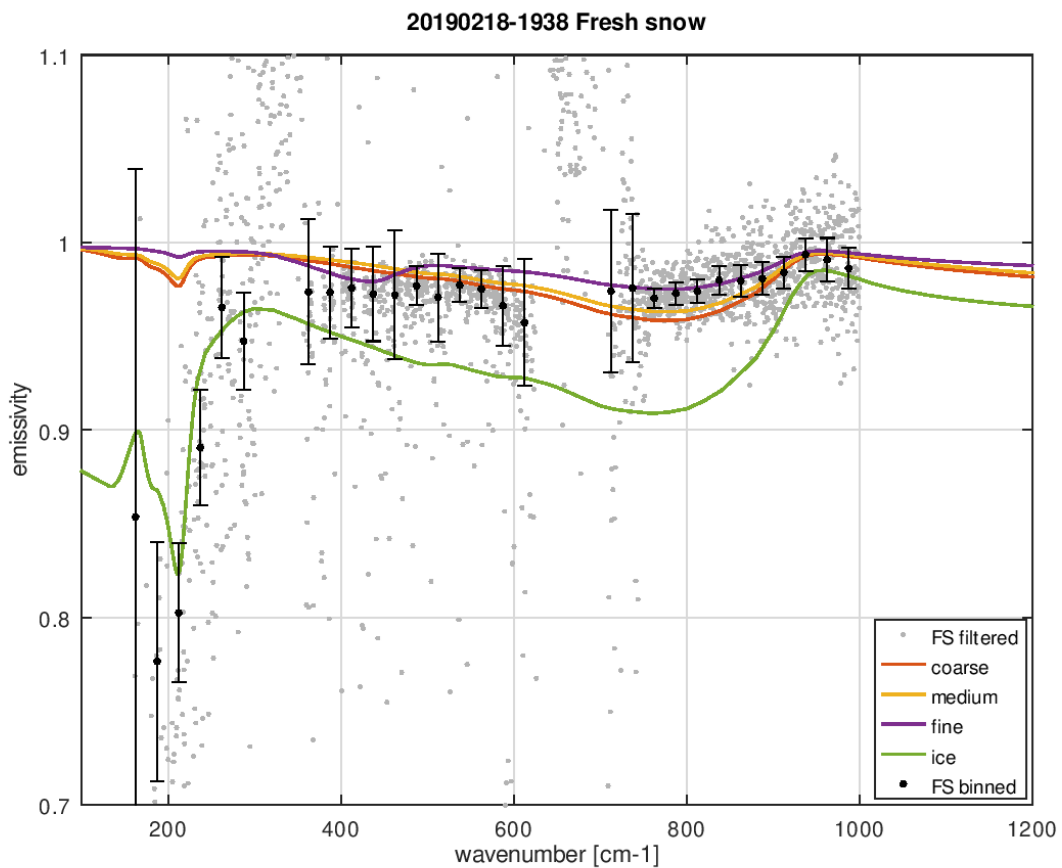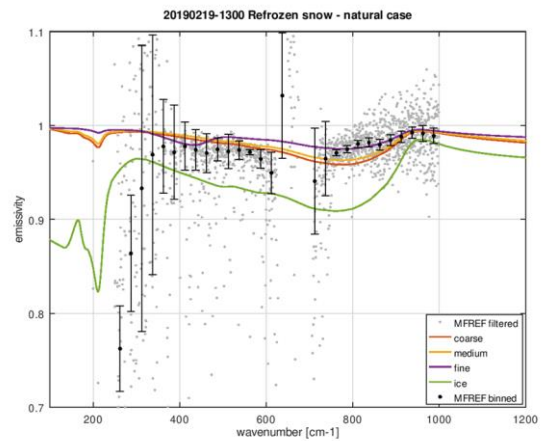*Figure 32 Emissivity values filtered and averaged in 25cm-1-wide bins.*
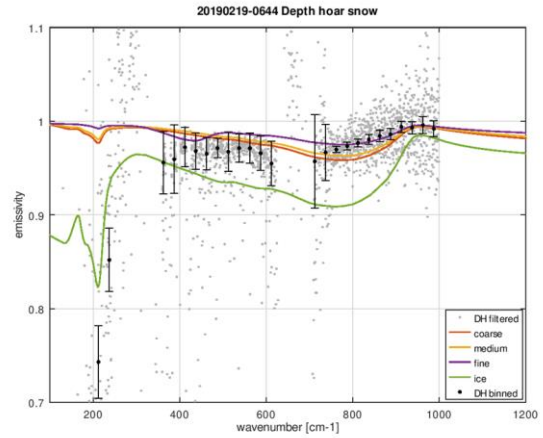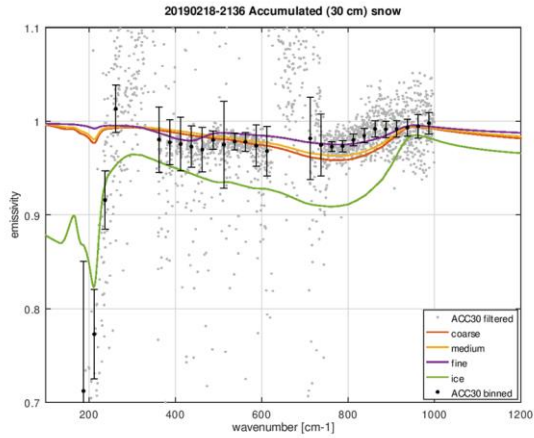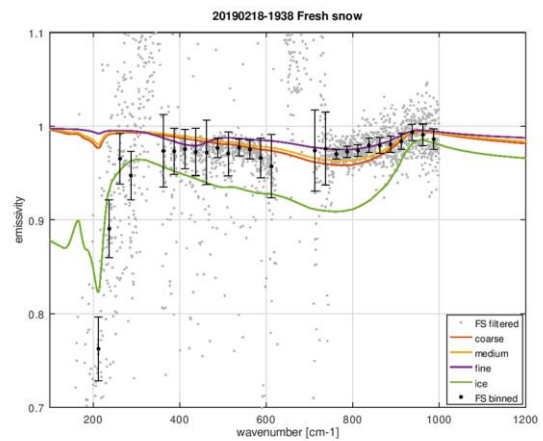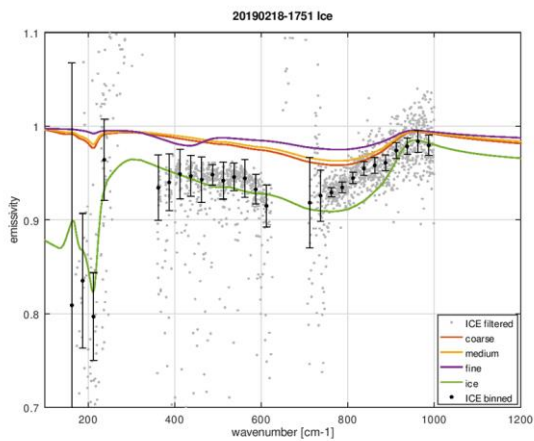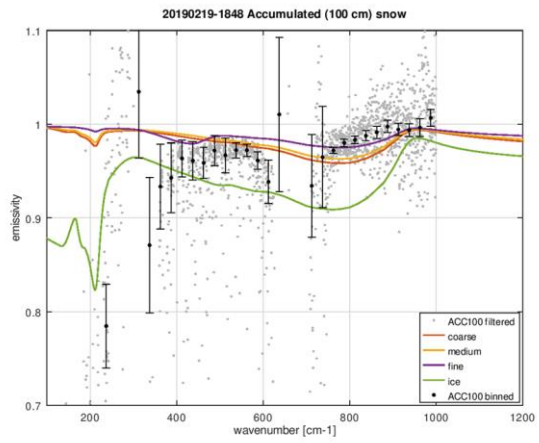
Figure 32 shows the result of the filtering and averaging process; the coloured continuous lines are surface emissivity values for ice and 3 diffdiverse typessnow from (Huang, Chen, Zhou, & Liu, 2016).

7.3 DETAILED RESULTS
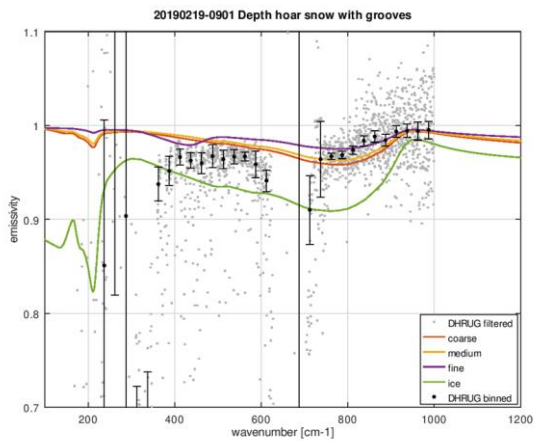
8 ANALYSIS OF FIRMOS MODIFICATIONS FOR AIRBORNE DEPLOYMENTS

The next improvement for FIRMOS is the deployment onboard aircraft or balloons. The aim is manifold. One purpose is to explore some features of the instrument operation at low (tens of mbar) or very low (few mbar) pressures. Then the specific design of some critical constituents, in order to survive shocks and vibrations, typical of take-off (aircraft, rockets) and landing (aircraft and balloons). Finally, an instrument similar to the satellite version could be useful for providing a ground-based support for intercalibration.

8.1 CONSTRAINTS

With respect to the ground operation at the top of Zugspitze, there are some different experimental conditions, which must be associated to the different platforms that can be used. The next table shows these different conditions.

	Ground	Aircraft	Balloon
Power	Unlimited	Sufficient	Strictly limited
Temperature	-20 ÷ +20 °C	-60 ÷ +35 °C	-80 ÷ +50 °C
Thermal insulation	Dynamic	Fixed	Fixed
Vibrations	Missing	Moderate	Negligible
Shocks	Missing	Moderate	Strong when landing
Attendance	Full time	Unattended	Unattended
Condensation	Negligible	Critical during descent	Critical during descent
Data transfer	No bandwidth limits	Strict bandwidth limit	Strict bandwidth limit
Line of sight orientation	Vertical upwards	Depends on location	Any but upwards

Let's examine them in details.

Power

On the ground, unless the station is a remote one, without a continuous power supply, there are no problems for power. Onboard an aircraft, the availability of power is usually sufficient, though at specific conditions (28 VDC, 115 V at 400 Hz). Onboard a balloon, only when solar panels are present there is an availability of power for the payload, and even in this case it is usually limited. In this case, a critical analysis of all the electric components is fundamental.

We can identify four main elements:

Computer. This is the easiest component to be adapted to low power operation. It is just a matter of deciding which are the tasks to be executed onboard. For sure, the computer must drive measurements and housekeeping recording, the movement of the field mirror and of the linear stage, data transmission to

ground. In principle, onboard data analysis is not necessary, so limiting the performance and power consumption of the CPU.

Blackbodies. At the moment the two blackbodies are kept at arbitrary temperature values by independent circuitries. This solution allows the maximum flexibility, but it's also the most demanding from the point of view of power.

Linear stage, field mirror actuator and two-channels controller. The power consumption of these items was impossible to be reduced when preparing the prototype for ground application. They represented a significant fraction of the total power consumption (tens of W).

Heaters. Heaters simply were two old style lamps, to be switched on and off according to the weather, and the level of implementation of an external thermal shield.

Temperature and thermal insulation

The problem of temperature derives from the increasing operating temperature range requested to the device, coupled to the absence of attending personnel. Moreover, while inside an aircraft the temperature is relatively stable (the reported range is outside the aircraft), onboard a balloon the excursion is really high.

Vibrations and shocks

Obviously, during ground operations there are no shocks, and even vibrations are practically negligible. On the contrary, aircraft and balloon operations feature quite different situations. When onboard aircraft, during flight, vibrations do exist, increasing at take-off, and are coupled with a shock at landing. On balloons, there are no vibrations (or at very low frequency) during the flight, some vibrations and a weak shock can occur at take-off, while a very hard shock (≥ 10 g) can be expected at landing, depending on dampers, inclination of the gondola at landing, and characteristics of the landing site.

Condensation

On the ground, the instrument can be easily protected against dew and other meteorological events. Onboard both aircraft and balloons, during the ascent the instrument is warmer than the external air, and anyway above tropopause the mixing ratio of water is below 10^{-4}. But, when descending, the instrument is substantially colder than external air, which can be very humid, depending on latitude and season. So, condensation on the instrument cannot be avoided.

Data transfer

Data links onboard any flying device are limited in bandwidth. It's necessary to reduce the amount of data transmitted to the ground.

Line of sight orientation

On the ground we have chosen to look at zenith. The orientation of the line of sight depends on the rack which the instrument is lying on. Onboard an aircraft the access to the exterior of the casing is limited, and moreover the orientation of the plane directly affects the field of view. Onboard a balloon, looking at nadir is the safest condition, as the gondola can rotate along the vertical axis. Any other orientation of the line of sight is unstable, unless the gondola is equipped with devices which allow to set its orientation.

8.2 IMPLEMENTATION PLAN

Power

As for power requirements here follow the specific actions.

Computer. A commercial embedded device is easily selectable in the market, suitable for application in absence of atmosphere, resistant to the shock typical of this application, and with a power consumption < 5 W.

Blackbodies. A possible implementation, to be verified by using a suitable simulation, is to connect the two blackbodies, so that the heat removed from the cold BB is directly transferred to the hot BB. Of course, the absolute temperatures cannot be controlled, only their difference can be set.
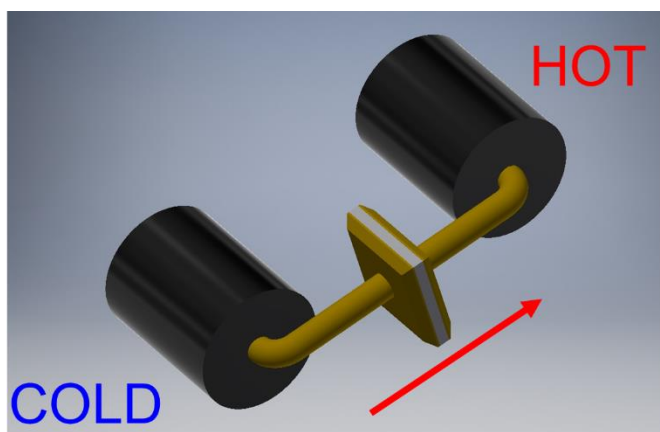
The simulation should assess whether the temperature excursion due to the external conditions is compatible with the requirements of the measurement, and how much power can be saved in this way.

Linear stage. A detailed market survey will be carried out, together with the analysis of the mechanical modifications, in order to understand which are the minimum capabilities required to this component. In particular, it's important to know the (approximate) weight of the roof mirrors holder, if it's possible to implement a safety device for take-off and landing, to be released during flight, and so on. Whatever the solution, the characteristics of payload weight, total elongation, speed, linearity, and resolution should be maintained.

Heaters. With a proper design, they should be not necessary any more, in particular onboard balloons, where power consumption of heating is a severe problem. A great care will be taken in thermal design, in order to eliminate the need of adding power inside the instrument.

Temperature and thermal insulation

It is relatively easy to provide the instrument with an effective thermal shield, with no requirements on power. On the contrary, expelling heat can be difficult or even impossible. Passive cooling requires a radiator, to be located in the shadow. Onboard a balloon this is possible only if the radiator is below the gondola (which means that it will break at landing), or if the whole gondola can be rotated, to be itself the shield of the radiator against sun. The latter feature is heavily demanding for the gondola. According to the payload (e.g.

telescopes, limb observing instruments, etc.), structures can be chosen, which allow orientation. But this is not the standard, so it's a good policy to be ready to any experimental condition.

Anyway, for what said at the beginning of this paragraph, night flights, or winter polar flights would be preferable, also as sun is not necessary for the observations of the instrument.

Vibrations and shocks

This is one of the key issues of the airborne operation. It's necessary to keep dimensions and weight as low as possible, but at the same time other features must be guaranteed: optical alignment against thermal stresses, and integrity of the whole device against all the mechanical perturbations, in particular balloon landing. This will require, first of all, a deep analysis of all the mechanical constraints, and of the maxima levels of shocks. The final redesign of the instrument will require a FEM analysis for both thermal and mechanical stresses.

Condensation

The protection of the inner side requires that the instrument can be sealed during descent, with on purged inlet only for air. This inlet should contain a drying filter, so that incoming air can be deprived of water. Of course, all this means that a shutter is installed at the viewing port, with suitable mechanical and vacuum properties.

Data transfer

Transmitting housekeeping data requires about 200 B/s. Transmitting spectra is much more demanding, as each acquisition consists of 14 MB. So, even one spectrum per hour would require about 4 kB/s. During airborne operation one or two spectra per hour are probably the limit allowed by the aircraft or gondola operation. Nevertheless, this transmission is important for an ultimate check of the instrumental behavior.

Line of sight orientation

Looking in different directions could be useful for several reasons. First of all, the aircraft or balloon is not above the atmosphere, but somewhere in the upper troposphere or in the stratosphere. This mean that a residual layer of air is above the instrument. It would be interesting to look both at nadir and at zenith, to take into account all the atmospheric layers. Also, limb observations could yield meaningful results. Unfortunately, looking in two opposite directions is relatively easy, but obliquus directions could be prevented by the presence of blackbodies. Moreover, onboard a balloon the zenith observation is impossible, and onboard aircraft several viewports would be necessary. So, an analysis will be done about the compatibility of different orientations of the line of sight and the mechanics of both the instrument and the platform.

8.3 DEPLOYMENT OPPORTUNITIES

We carried out a survey about the possibilities of deployment for a balloon version of FIRMOS. We already have experience of balloon deployment for a gas analyser, in the frame of the HEMERA Project (https://www.hemera-h2020.eu/page-d-exemple/). HEMERA provides free launch opportunities for scientific payloads. We explored availability and schedule of calls within this particular frame. A call was available, with deadline Dec. 13, 2019, for flights in 2021. We applied, stating that the prototype needs developments for deployment onboard a balloon, and that we are finding agreements about funds with

national and international agencies. The selected kind of balloon, among the available types, is Zero Pressure Balloon, because of payload weight and flight altitude. For this kind of platform, the available launch sites are Timmins (CA), and Kiruna (S). Selection of experiments is on the basis of scientific validity and readiness of the hardware (or available funds and time for development). The assignment of a payload to a mission is based on overall weight of the payload, special needs about gondola orientation, flight altitude and duration, requested date and daytime/night-time of flight. Evaluation of the applications is in progress.

9 ABBREVIATIONS

BB (black Body).
BS (Beam splitter).

CalErr (calibration errors).
CBB (Cold black body).
COBALD (Compact Optical Backscatter Aerosol Detector),.

De (ice particle equivalent diameter). ,
DLATGS (deuterated, L-alanine doped triglycine sulphate).
DLR (downwelling longwave radiation).
DOF (degrees of freedom).
DUFISSS (DUal Frequency Integrating Sphere for Snow SSA).
DWD – CDC (Deutscher Wetterdienst Climate Data Center).

E-AERI (Extended-range Atmospheric Emitted Radiance Interferometer).

FIR (far-infrared).
FIRMOS (Far-Infrared Radiation Mobile Observation System).
FM (Forward Model).
FORUM (Far-infrared-Outgoing-Radiation Understanding and Monitoring).
FOV (Field of view).
FTS (Fourier transform spectrometer).

HBB (Hot black body).

ISRF (Instrumental spectral response function), 20
IWP (Ice Water Path).
IWV (Integrated Water Vapour).

KLIMA ((Kyoto protocoL and Informed Management of the Adaptation).

LWP (Liquid Water Path).

NESR (Noise equivalent spectral radiance).
NLSF (Nonlinear Least Square Fit).

OD (Optical Depth). ,

PDU (Pyroelectric Detector Unit).
PET (Polyethylene terephthalate).
PV (peak-valley).

D8 "Final Report"	Doc. name: FIRMOS D8 final report
ESA Contract No. 4000123691/18/NL/LF	Rev.: v3.6 - final
	Date: 10 April 2020
	Page: 46/48

RBB (Reference black body).
REFIR-PAD (Radiation Explorer in the Far InfraRed – Prototype for Applications and Development),.
RM (Retrieval Model)..

SACR (Simultaneous Atmospheric and Cloud Retrieval).
SSA (Specific Surface Area).

UFS (Environmental Research Station Schneefernerhaus).

VCM (Variance Covariance Matrix).

10 REFERENCES

Bellisario, C., Brindley, H. E., Murray, J. E., Last, A., Pickering, J., Harlow, R. C., & … Chen, X. (2017). Retrievals of the Far Infrared Surface Emissivity Over the Greenland Plateau Using the Tropospheric Airborne Fourier Transform Spectrometer (TAFTS). *Journal of Geophysical Research: Atmospheres, 122*(22), 12152-12166. doi:10.1002/2017JD027328.

Bianchini, G., Palchetti, L., Carli, B., (2009). Vectorial combination of signals in Fourier transform spectroscopy. *Infrared physics & technology* 52 (1), 19-21. doi: 10.1016/j.infrared.2008.09.004.

Bianchini, G. and Palchetti, L., (2008) Technical Note: REFIR-PAD level 1 data analysis and performance characterization, Atmos. Chem. Phys., 8, 3817–3826, doi:10.5194/acp-8-3817-2008.

Carli, B., Palchetti, L., Raspollini p. (1999). Effect of beam splitter emission in Fourier-transform spectroscopy, *Applied Optics* 38 (36).

Cortesi, U., Del Bianco, S., Gai, M., Laurenza, L. M., Ceccherini, S., Carli, B., Buchwitz, M. (2014). Sensitivity analysis and application of KLIMA algorithm to GOSAT and OCO validation - KLIMA-IASI. *IFAC-TSSR, 6* (Final Report of Project ESA-ESRIN/Contract n. 21612/08/I-OL), 1-153.

Di Natale, G., Palchetti, L., Bianchini, G., & Del Guasta, M. (2017). Simultaneous retrieval of water vapour, temperature and cirrus clouds properties from measurements of far infrared spectral radiance over the Antarctic Plateau. *Atmospheric Measurement Techniques, 10*(3), 825-837. doi:10.5194/amt-10-825-2017.

Dirksen, R. J., Sommer, M., Immler, F. J., Hurst, D. F., Kivi, R., and Vömel, H. (2014). Reference quality upper-air measurements: GRUAN data processing for the Vaisala RS92 radiosonde, *Atmos. Meas. Tech.*, 7, 4463–4490, doi:10.5194/amt-7-4463-2014.

Huang, X. L., Chen, X. H., Zhou, D. K., & Liu, X. (2016). An observationally based global band-by-band surface emissivity dataset for climate and weather simulations. *Journal of the Atmospheric Sciences, 73*, 3541-3555. doi:10.1175/JAS-D-15-0355.1.

Klett J.D, (1981). Stable analytical inversion solution for processing lidar returns. *Applied Optics*, 20 (2).

Kochanov, R., Gordon, I., Rothman, L., Wcislo, P., Hill, C., & Wilzewski, J. (2016). HITRAN Application Programming Interface (HAPI): A comprehensive approach to working with spectroscopic data. *J. Quant. Spectrosc. Radiat. Transfer, 177*, 15-30. doi:10.1016/j.jqsrt.2016.03.005.

Palchetti, L., Barbis. A., Harries, J. E., Lastrucci, D. (1999). Design and mathematical modelling of the space-borne far-infrared Fourier transform spectrometer for REFIR experiment. *Infrared physics & technology*, 40 (5), 367-377. doi: 10.1016/S1350-4495(99)00026-2.

Sussmann, R., Reichert, A., and Rettinger, M. (2016). The Zugspitze radiative closure experiment for quantifying water vapour absorption over the terrestrial and solar infrared – Part 1: Setup, uncertainty analysis, and assessment of far-infrared water vapour continuum, *Atmos. Chem. Phys.*, 16, 11649-11669, doi:10.5194/acp-16-11649-2016.

Yang, P., Bi, L., Baum, B. A., Liou, K.-N., Kattawar, G. W., Mishchenko, M. I., & Cole, B. (2013). Spectrally Consistent Scattering, Absorption, and Polarization Properties of Atmospheric Ice Crystals at

Wavelengths from 0.2 to 100 μm. *Journal of the Atmospheric Sciences, 70*(1), 330-347. doi:10.1175/JAS-D-12-039.1